Fragmentation and energy dissipation in rockfall: Effects of block shape and non-collinear impact dynamics

International Journal of Rock Mechanics & Mining Sciences 198 (2026) 106381

Contents lists available at ScienceDirect

International Journal of Rock Mechanics and Mining Sciences

journal homepage: www.elsevier.com/locate/ijrmms

Research paper

Fragmentation and energy dissipation in rockfall: Effects of block shape and non-collinear impact dynamics

Maddalena Marchelli [a,*], Davide Ettore Guccione [b], Anna Giacomini [b], Olivier Buzzi [b]

[a] Department of Environment, Land and Infrastructure Engineering (DIATI)- Politecnico di Torino, C.so Duca degli Abruzzi 24, I–10129 Torino, Italy
[b] Centre for Geotechnical Science and Engineering, College of Engineering, Science and Environment, University of Newcastle, University Dr, 2308 Callaghan, NSW, Australia

ARTICLE INFO

Keywords:
Non-collinear impact
Fragmentation in rockfall
Restitution coefficient
Trajectories
Block shapes

ABSTRACT

Understanding fragmentation and energy dissipation during rockfall events is essential for accurate hazard assessment and predictive modelling. To date, most experimental studies have used spherical specimens, primarily because of their geometric simplicity and ease of repeatable testing. This work investigates the dynamic behaviour of angular block shapes, i.e., cubes, prisms, and slabs, which more closely resemble natural rock geometries, through free-fall drop tests up to 10 m/s, complemented by static splitting tests to explore potential links with dynamic response. These geometries often result in non-collinear impacts with multiple contact points and prolonged impact durations, significantly influencing the likelihood of fragmentation and post-impact dynamics. The study examines how block geometry, impact orientation and location (face, edge, vertex) affect failure patterns and energy restitution.

Results show that fragmentation probability strongly depends on geometry: slabs fragmented in 33% of tests, prisms in 50%, while cubes only at the highest velocity. Static tests revealed geometry- and loading condition- dependent tensile strength, with prisms showing the highest median value (≈ 2.3 MPa) and slabs the lowest (≈ 1.1 MPa). Fragmentation severity also varied, with slabs producing finer fragments compared to prisms. For intact specimens, apparent restitution coefficients ranged from 0.13 (prisms) to 0.39 (cubes), significantly lower than spheres (≈ 0.34), and impact durations were up to two orders of magnitude longer than for spherical blocks. The results highlight the complex interplay between block geometry, impact conditions, and energy dissipation, providing shape-dependent metrics for improving rockfall trajectory models.

1. Introduction

Rockfall is a high-energy, gravity-driven process involving the detachment, free fall, and successive impacts of rock blocks along steep natural or engineered slopes. These events pose significant hazards to infrastructure, transportation corridors, and human life in mountainous regions.[1,2] The kinematic behaviour of falling blocks, including translational and rotational motion, fragmentation, impact-induced energy dissipation, and rebound trajectories, critically influences subsequent propagation, runout distances, and impact forces.[3–5] Accurate prediction of rockfall behaviour requires a detailed understanding of both the mechanical response of blocks upon impact and the energy transfer mechanisms that govern fragmentation and post-impact motion.[6] While substantial progress has been made in modelling rockfall kinematics, understanding of fragmentation mechanisms and post-impact dynamics remains limited, particularly for blocks with realistic geometries.[7,8]

Dynamic impact tests, particularly free-fall and parabolic drop tests, have been widely employed to simulate rockfall events and investigate fragmentation thresholds, energy dissipation, and rebound behaviour.[9–18] A key parameter in such studies is the coefficient of restitution (CoR), defined as the ratio of rebound velocity to impact velocity, which quantifies the energy retained after impact. The CoR is now routinely incorporated into rockfall trajectory models to estimate post-impact velocities and angles.[19–21] While laboratory experiments provide controlled conditions for isolating specific variables, most experimental and related numerical investigations have predominantly focused on spherical specimens.[22,23] which offer geometric simplicity and predictable contact behaviour. Spheres tend to generate collinear impacts with well-defined stress distributions, which makes them ideal for repeatable studies but less representative of the irregular and angular blocks typically involved in natural rockfall events.[24] Some laboratory studies have explored the influence of block shape,[10,25] but they have primarily focused on its effect on the coefficient of restitution, without addressing other critical aspects such as contact duration, detailed post-impact motion, and fragmentation behaviour. Several

* Corresponding author.
E-mail address: maddalena.marchelli@polito.it (M. Marchelli).

https://doi.org/10.1016/j.ijrmms.2025.106381
Received 12 September 2025; Received in revised form 14 November 2025; Accepted 7 December 2025
Available online 11 December 2025

numerical studies have similarly focused on kinematic aspects without incorporating fragmentation. For instance, Krengel et al.[26] used 2D discrete element method (DEM) simulations to show that block shape and initial orientation significantly influence runout and restitution coefficients, with outcomes highly sensitive to even minor variations in geometry or launch conditions. Similarly, Dattola et al.[27] proposed a rheological model for ellipsoidal block impacts that accounts for eccentricity, rotation, and impact angle, offering a refined approach to restitution analysis by considering non-point-like contacts; however, their work did not address fragmentation. In contrast, other studies have explicitly examined fragmentation, focusing on fracture outcomes and energy dissipation. In detail, investigations on concrete armour units and engineered blocks[28,29] have demonstrated that block geometry and impact configuration strongly affect breakage. Das et al.[30] explored how block shape influences fracture patterns and energy dissipation during impact, while Ye et al.[31] employed DEM simulations to assess the effects of elongation and flatness ratios on dynamic breakage, including rebound and post-impact motion. Nevertheless, these simulations commonly assume planar, horizontal contacts and do not account for inclined impacts or multiple simultaneous contact points, thereby limiting the realism of contact dynamics in rockfall scenarios.

Only a limited number of in situ tests have been conducted to capture the complexity of real-scale rockfall dynamics, including irregular terrain, natural block geometries, and heterogeneous surface conditions,[32–34] but their interpretability is often constrained by the variability in block shape and impact conditions, which introduces significant scatter in motion parameters. Recent advances in experimental techniques, including high-speed imaging, multi-view photogrammetry, and 3D scanning technologies, have enabled more detailed investigations of fragmentation processes and post-impact motion.[35–37]

Although some rockfall trajectory models now incorporate shape-dependent rolling and bouncing behaviour,[38–40] they rarely account for fragmentation or non-collinear impact effects, limiting their predictive accuracy. Fragmentation is often treated as a binary outcome or modelled using empirical rules, without addressing the underlying mechanics of failure or the influence of block shape and contact dynamics.[41,42] While a few models do include fragmentation processes,[43–46] they are generally limited to spherical blocks or rely on lumped-mass representations that fail to capture the geometric complexity and contact variability inherent to angular rock blocks. Notably, Guccione et al.[46] proposed a fragmentation model based on survival probability, offering a more robust criterion, though still limited to spherical blocks.

This study aims to provide new insights into the fragmentation processes and energy dissipation of brittle blocks with geometries that approximate real rock shapes. To this end, the study focuses on three distinct specimen geometries, i.e., prisms, cubes, and slabs, selected to ensure repeatability and minimising geometric variability. Although the experimental setup, i.e., free fall drop tests on artificial mortar specimens, represents a simplification of natural rockfall events, it enables controlled exploration of shape-dependent failure mechanisms. The primary objective is to understand how block geometry, impact orientation and location (face, edge, vertex) influence fragmentation patterns, interaction (number, duration, and sequence of contacts), and post-impact dynamics. To complement the dynamic tests, a targeted series of static splitting tests (indirect tensile tests), encompassing both conventional and non-standard configurations, was conducted to characterise quasi-static fracture behaviour. These tests, under controlled conditions, aim to identify geometry-driven stress concentrations and fracture modes that may affect fragmentation occurrence and rebound behaviour in the free-fall cases. Although numerical modelling is essential for predictive purposes, this study focuses specifically on controlled experiments to isolate the effect of block geometry and non-collinear impacts. The resulting dataset provides a benchmark for future numerical validation.

2. Methodology

2.1. Experimental setup

2.1.1. Dynamic tests: free-fall drop tests

A series of vertical free-fall drop tests was carried out using the fragmentation facility developed at the University of Newcastle[47] (Fig. 1.a). The enclosed hexagonal chamber is equipped with a fibre-reinforced concrete slab, a vacuum-based release mechanism, and a high-speed imaging system comprising six externally mounted cameras, i.e., two Phantom VEO-E340L cameras and four Optronics. This configuration enables the capture of the free-fall, impact, rebound, and fragmentation phases of the specimens. Images were recorded at 500 frames per second, with exposure times of 500 μs for the Optronics and 100 μs for the Phantom cameras. Specimens were lifted using a vacuum tube and pulley system, suspended from the roof structure of the building. Specimens were positioned in the vacuum-release mechanism to achieve different impact configurations (face, edge, or vertex) and orientations relative to the slab surface, then released smoothly by disengaging the vacuum. The maximum drop height is 5.1 m, which results in a maximum impact velocity of about 10 m/s. After each test, all the samples, or all fragments in case of fragmentation, were recorded, collected and weighted.

2.1.2. Static test: diagonal splitting and vertex-to vertex loading tests

During the static testing campaign, displacement-controlled compression tests were conducted using a servo-hydraulic MTS Criterion testing machine (maximum load capacity: 300 kN) with a spherical seat, operated at a constant rate of 5 mm/min (Fig. 1.b). Force–displacement data were recorded for each test. A high-resolution video camera Nikon D800e (frame rate: 30 fps, resolution: 1.920 × 1.080 pixel) was positioned laterally to capture the evolution of fracture patterns and crack propagation in real time.

Two distinct loading configurations were adopted to investigate the fracture behaviour of geometrically diverse specimens (prisms, slabs, and cubes). The first involved diagonal splitting tests, in which compressive loads were applied along opposing edges to induce tensile failure along oblique planes. This configuration deviates from conventional Brazilian-type tests[48] or standard splitting tensile strength methods,[48–52] which typically apply diametral compression to cylindrical specimens or concentrated loading along a narrow strip on the lateral face of prismatic or cubic specimens. Although less commonly used, diagonal configurations have previously been explored in the literature for cubic specimens,[53–57] demonstrating its relevance for assessing tensile failure under complex loading paths. The second configuration consisted of vertex-to-vertex loading, where compressive forces were applied at opposing corners of the specimens. This setup mimics the point load test used in rock mechanics,[58,59] generating highly localised stress concentrations at the vertices.

The rationale for employing these two complementary configurations lies in their ability to probe different aspects of the material's mechanical response under quasi-static conditions. The diagonal splitting tests were designed to promote oblique fracture planes and induce non-uniform tensile stress fields, enabling a comparative assessment of failure mechanisms across different shapes. In contrast, the vertex-to-vertex tests focused on stress localisation and vertex fragility, capturing the onset of fracture under extreme boundary conditions. Together, these configurations provide insight into geometry-driven stress redistribution and crack initiation. It is important to note that these static tests were meant to serve as a preliminary investigation into the fracture behaviour of the material. While limited in scope, they provide a foundational understanding of failure mechanisms and stress localisation effects, which can meaningfully inform the interpretation of more complex dynamic impact responses examined in subsequent phases of the study.

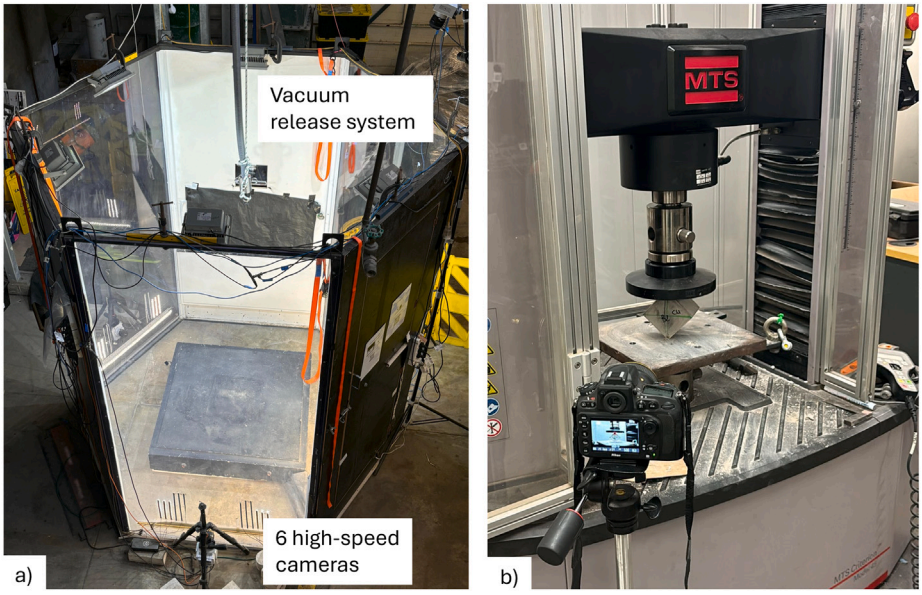

Fig. 1. Experimental setup comprising: the fragmentation cell (a) and the servo-hydraulic MTS testing machine (b).

2.2. Data analysis

2.2.1. Impact data from image analysis

All high-speed image sequences were analysed using TEMA3Ds software[60] to extract key impact parameters, following the calibration procedure described in Guccione et al.[47] For each test, the impact location was classified as occurring on a face, edge, or vertex, while the impact orientation was defined by the three angles θ formed between the three orthogonal faces of the specimen converging at the impact point (A) and the impacted surface. In cases where the contact occurs on an edge or a face, A is defined as the midpoint of the respective edge or face. Fig. 2 presents a schematic of a generic specimen impacting the target surface. The three planes defined by the vertices A-B-C, A-B-D, and A-C-D represent the three orthogonal faces from which the angles with the impacted surface, namely θ_{ABC-z}, θ_{ABD-z}, and θ_{ACD-z}, are computed. Some conventions were adopted: for prismatic specimens, the edge A–D corresponds to the longest edge, whereas for slab-like specimens, A–B represents the shortest edge (Fig. 3).

Fragmentation was systematically assessed for each test. The presence, extent (number of fragments), and type of fragmentation, ranging from minor chipping to complete breakage, were identified through frame-by-frame analysis of high-speed footage and post-impact specimen inspection.

The nature of the specimen/impacted surface interaction was further analysed in terms of impact duration, number and sequence of contact points (or edges or surfaces) occurring during the first impact event. In the case of collinear impacts, typically observed in spherical specimens, the contact with the ground surface is point-like, involving a single contact point and a brief interaction before rebound, sliding, or rest. In contrast, specimens with angular or elongated geometries often exhibit complex interaction during the initial impact, involving multiple sequential contacts on vertices, edges, and faces. These multi-contact configurations extend the duration of the impact and reflect the body's search for a stable post-impact configuration. To quantify this, we defined the impact duration t_I as the time interval during which the centre of gravity remained at or below its position from the preceding instant, without sliding or coming to rest. This ensures that only the active contact phase is considered, ending when the centre of gravity begins to rise. All contact events occurring within this interval were considered part of a single impact and the moment the centre of gravity begins to rise marks the onset of rebound and the end of the impact phase. For each test, the number of distinct contact events prior to

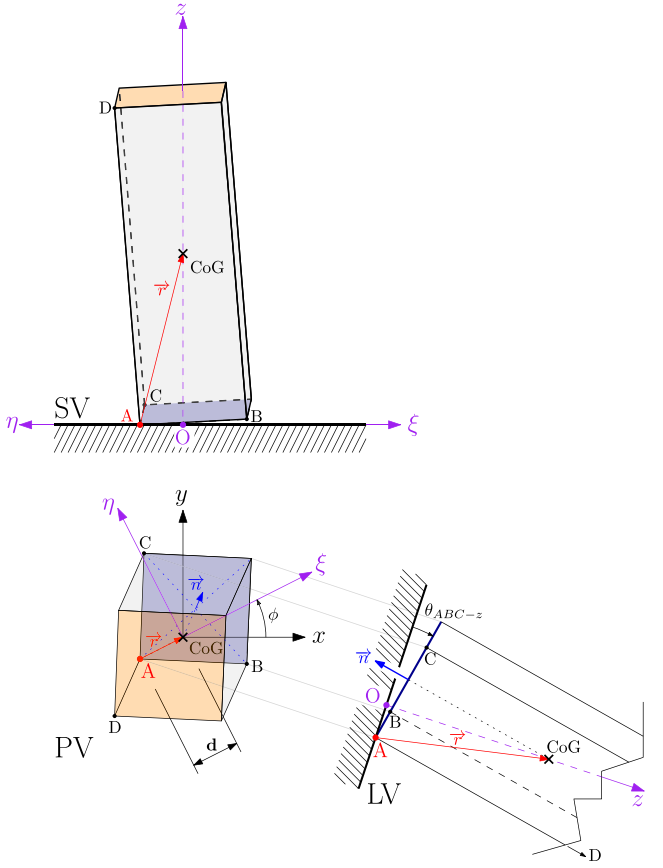

Fig. 2. Sketch of the local reference system. A generic specimen impacting the target surface is shown. SV = side view; PV = plan view; LV = lateral view. Point A indicates the impact location, while CoG denotes the centre of gravity. The global and local reference systems are represented by x–y–z and ξ–η–z, respectively.

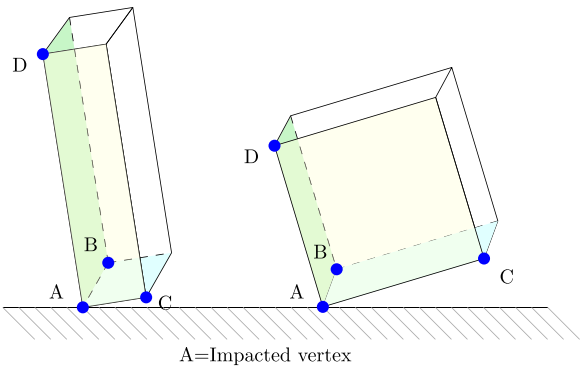

Fig. 3. Sketch of the *A-B-C*, *A-B-D*, and *A-C-D* planes for prism and slab-like specimens. Point *A* indicates the impact point.

rebound, sliding, or rest was manually counted through frame-by-frame image analysis, allowing an estimate of the total impact duration t_I (Fig. 4). This metric is particularly relevant for propagation modelling, where impact duration influences energy dissipation and post-impact motion.

Sample motion was analysed using TEMA3Ds software.[60] The software employs an outline tracking algorithm to reconstruct 3D trajectories from multi-view silhouettes. The rebound and post-impact trajectories of non-fragmented samples were tracked to evaluate the coefficient of restitution and investigate the influence of sample shape on energy dissipation and motion. Fragment tracking was not performed at this stage, as the current study focuses on the dynamics of intact specimens. Due to the complexity of fragment motion, characterised by irregular geometries, rapid rotations, and frequent visual obstructions, quantitative tracking of individual fragments is deferred to a subsequent phase of the research. At this stage, fragmentation was assessed qualitatively through visual inspection of the high-speed footage.

Tracked tests were post-processed in MATLAB[61] to examine the trajectories and analyse the influence of block shape, impact orientation and location on post-impact dynamics. The global reference system (Oxyz) used to track the specimens was centred at the middle of the impact plane, with the x–y axes lying on the target surface and the z axis oriented normal to it along the trajectory of the centre of gravity of the falling mass. To enable consistent comparison across tests, a local reference system (O$\xi\eta z$) was defined for each specimen, centred at the projection of its centre of gravity (CoG) onto the impact plane. The vector $\vec{r}$, connecting the impact point A to the specimen's centre of gravity (CoG), was used to define the orientation of the local reference system. Specifically, the direction of the ξ-axis was defined in such a way that the corresponding unit vector $\vec{i_\xi}$ is oriented along the projection of $\vec{r}$ onto the global x–y plane. The η-axis, orthogonal to ξ, lies within the x–y plane and is defined as positive in the anti-clockwise direction from ξ. The z-axis remains aligned in both the global and local reference systems. The angle ϕ, which determines the rotation between global and local reference systems, is defined as the positive anti-clockwise angle between the unit vectors $\vec{i_x}$ and $\vec{i_\xi}$, and is computed as:

$$\vec{i_\xi} \cdot \vec{i_x} = \cos\phi. \tag{1}$$

The impact eccentricity d is defined as the length of the projection of $\vec{r}$ onto $\vec{i_\xi}$, i.e., the distance between the impact point A and the projection of the CoG onto the impact plane, measured along the ξ-axis:

$$d = \vec{r} \cdot \vec{i_\xi}. \tag{2}$$

Accordingly, the post-impact velocity components transform as follows:

$$v_x = \cos\phi v_\xi - \sin\phi v_\eta \tag{3}$$

$$v_y = \sin\phi v_\xi + \cos\phi v_\eta, \tag{4}$$

while v_z remains unchanged.

The choice of this local reference system lies in the mechanics of the initial interaction between the block and the impacted surface. Upon contact, an upward reaction force is generated at the impact point. Since this force is not collinear with the inertial force acting through the centre of gravity (CoG) of the falling body, a moment is induced. This moment initiates the first rotational motion of the specimen during the impact phase. The moment vector is oriented normal to the plane defined by the vector $\vec{r}$, connecting the impact point to the CoG, and the global vertical axis (z-axis).

To analyse the rebound direction, two angles were defined in the local reference system (O$\xi\eta z$). The planar angle β is measured clockwise between the η-axis and the post-impact velocity vector projected onto the ξ–η plane. This angle captures the directionality of rebound motion relative to the specimen's geometry. Trajectories aligned with the positive ξ-axis correspond to $\beta \approx 90°$, indicating motion predominantly along the line connecting the impact point to the CoG. Additionally, the vertical projection angle α is defined between the vertical velocity component (v_z) and the horizontal velocity magnitude in the ξ–η plane, computed as $\sqrt{v_\xi^2 + v_\eta^2}$. This angle quantifies the proportion of vertical motion relative to horizontal motion, providing insight into energy dissipation and rebound potential. Both angles are illustrated in Fig. 5.

Whereas traditional trajectory models typically treat the block as a material point and rely solely on restitution coefficients to encapsulate impact behaviour, our approach acknowledges that these coefficients implicitly include effects such as rotational exchange, and multiple contacts, consistent with the extended modelling frameworks proposed by Vijayakumar et al.[62] and Dattola et al.[27] Accordingly, we computed an apparent restitution coefficient, evaluated with reference to the CoG, as the ratio between is the translational velocity at the end of the impact v_e and the incident impact velocity v_i.

Rotational motion was not quantitatively analysed in this phase. This decision was guided by several considerations. The primary objective of the current phase was to isolate the influence of shape and contact configuration on translational energy dissipation and rebound behaviour in intact specimens. In the context of apparent restitution analysis, the rotational contribution is implicitly embedded in the post-impact translational velocity of the centre of gravity, as discussed in Dattola et al.[27] This approach aligns with the assumptions commonly adopted in lumped-mass trajectory models, where the block is treated as a single mass point and rotational effects are not explicitly resolved but are instead incorporated into effective translational parameters. Therefore, while rotation undoubtedly influences energy redistribution during impact, its explicit quantification is deferred to a subsequent phase of the study, where enhanced tracking protocols and higher-resolution imaging will be employed.

2.2.2. Static test analysis

High-resolution video footage was used to qualitatively classify fracture types, including single cracks, multiple branching cracks, and localised crushing at contact points, giving attention to identifying crack initiation zones and tracking propagation paths, where visible, to understand how stress redistributes across different geometries and loading configurations. Fracture patterns were correlated with specimen shape (cubes, slabs, prisms) and loading type (diagonal edge-to-edge vs. vertex-to-vertex) to explore how geometry influences failure mechanisms. For each test, the symmetry of crack propagation was qualitatively assessed based on visual inspection. Fractures were considered symmetric when crack development occurred in a mirrored fashion on either side of the loading axis. In contrast, asymmetric fractures were identified by uneven crack propagation, branching, or deviation from the expected path. Special attention was given to linking the observed static fracture features to the dynamic behaviour of the same specimen types under drop-weight impact. In particular, the presence of vertex fragility, oblique cracking, or asymmetric fracture

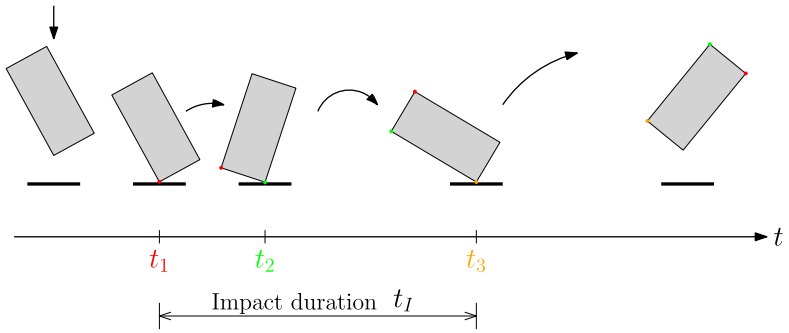

Fig. 4. Schematic representation of impact duration t_I and contacts sequence during the first impact event. The interval t_1 to t_3 defines the active contact phase, during which the specimen's CoG remains at or below its position from the preceding instant. After t_3, the CoG begins to rise, marking the end of the impact and the onset of rebound. All contact events occurring within this interval are considered part of a single impact.

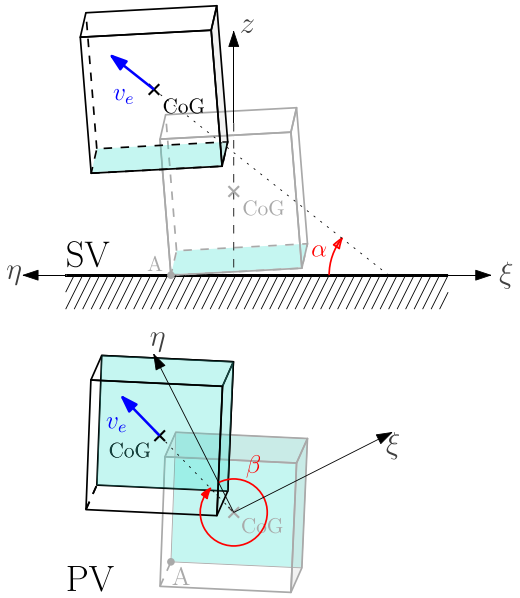

Fig. 5. Sketch of a post-impact specimen with its velocity vector, highlighting the angles α (front view, top part of the figure) and β (plane view, bottom part of the figure). For simplicity, no rotation of the specimen and a unique contact is considered during the impact time t_I. SV = side view; PV = plan view.

in static tests was evaluated as potential indicators of fragmentation propensity in dynamic conditions.

Force–displacement curves obtained from the MTS machine were analysed to extract key mechanical indicators. While the initial slope of the curve can provide insight into the elastic stiffness of the specimen, the post-peak behaviour can allow to distinguish between brittle failure (sharp load drop) and more gradual softening, possible indicators of progressive damage or frictional effects along the fracture plane. The peak load F_p was identified as a measure of tensile strength or vertex resistance, depending on the loading configuration. To enable comparison across specimens of different sizes and shapes, for edge-to-edge configurations, an equivalent splitting tensile strength was computed by dividing the peak force F_p by the area associated with the fracture plane A_p:

$$\sigma_t \propto \frac{F_p}{A_p}. \tag{5}$$

Similarly, for vertex-to-vertex tests the tensile strength was estimated following the approach proposed by Hiramatsu and Oka,[63] who demonstrated that the tensile strength of rock can be approximated by:

$$\sigma_t = 0.9\frac{F_p}{D^2}, \tag{6}$$

where D is the distance between the loading points. Although this method does not produce a uniform stress field and is influenced by the material properties and geometry of the specimen, it provides a reasonable estimate of tensile strength under concentrated loading conditions. To account for geometric influences, Broch and Franklin[64] introduced a shape-dependent correction factor, applied multiplicatively to the vertex-to-vertex tensile strength formulation of Eq. (6), to account for geometric influences, typically ranging from 0.5 to 1.0 depending on the specimen's shape and dimensions. Given this variability, comparisons of tensile strength across different geometries (e.g., prisms, slabs, cubes) require careful consideration. Accordingly, the possibility of identifying a consistent conversion factor across specimen shapes was thus examined to support more robust interpretation of geometry-dependent fracture behaviour.

3. Material and experimental program

3.1. Material and specimen preparation

To ensure consistency and minimise the variability associated with natural rock materials, all specimens were cast from a mortar composed of silica sand, Portland cement, hydrated lime, and water, mixed in a mass ratio of 3:1:0.125:1. A cement accelerant (2% by weight of cement) was added to accelerate the curing process. Once cured, the mortar exhibited a density of approximately 2000 kg/m^3. This mixture was selected to replicate the material used in previous studies involving spherical specimens, thereby enabling direct comparison of fragmentation probability and energy dissipation characteristics across different geometries.[15,16] Guccione et al.[15] also tested different mortar compositions and observed that, while fragmentation probability varies with tensile strength, the general trends in fragmentation mechanisms and rebound behaviour remain consistent across mixtures. This suggests that block geometry effects on fragmentation and rebound can be considered independent of mortar composition, and it is reasonable to assume that similar trends will hold across different brittle materials.

The specimens were cast using custom-made PVC and wooden moulds (Fig. 6.a). After casting, the samples underwent a two-stage curing process: they were first cured for 14 days in a 100% humid environment, followed by 21 days of drying in a ventilated oven at 40 °C. Both the vertical drop tests and the static loading tests were performed immediately after the curing period to ensure consistent material conditions.

Because the specimens were produced in different batches, a comprehensive material characterisation campaign was carried out for each batch. This included Brazilian tensile strength (BT) tests,[48] unconfined compressive strength (UCS) tests,[65] and fracture toughness tests.[66] In

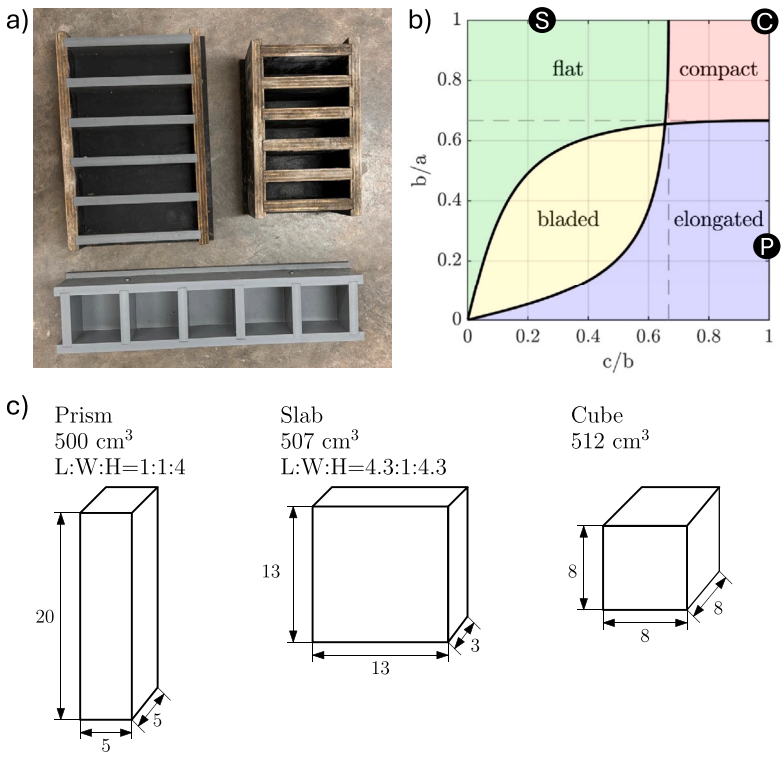

Fig. 6. (a) Custom-made PVC and timber moulds. (b) Classification of the prism, slab, and cube specimens used in this study, plotted on the particle form chart proposed by Angelidakis et al.[67]: solid lines denote the boundaries between bladed, elongated, compact, and flat particles according to Angelidakis et al. while dashed lines represent the Zingg classification system,[68] from which Angelidakis adapted the chart. Specimen dimensions follow the convention $a > b > c$, where a, b, and c denote the principal lengths of the specimen. (c) Schematic representation of the investigated specimen shapes (prisms, slabs, and cubes), with dimensions indicated.

Table 1
Characteristics of mortar mixtures. The values are presented as averages, with standard deviations indicated. The abbreviations 'sec' and 'tan' denote secant and tangent modulus, respectively.

Proportions: sand/cement/ lime/water	Young modulus (tan) (MPa)	Young modulus (sec) (MPa)	Unconfined compressive strength σ_c (MPa)	Tensile strength σ_t (MPa)	Fracture toughness K_{Ic} (MPa $m^{1/2}$)
3/1/0.125/1	2517 ± 369	1756 ± 253	17.40 ± 1.49	2.05 ± 0.34	0.3758 ± 0.070

total, 35 BT, 36 UCS, and 31 toughness tests were performed. The average values and standard deviations of the measured mechanical properties are reported in Table 1.

3.2. Experimental program

Three regular shapes, i.e., prisms, slabs, and cubes were selected to simulate angular rock blocks without internal discontinuities. All specimens have a volume of approximately 500 cm^3, enabling direct comparison across geometries and with previous studies on spherical specimens.[15,16] In particular, the reference sphere used in earlier work had a volume of 523 cm^3, i.e., a diameter of 10 cm, while the prism, slab and cube used in this study had volumes of 500, 507, and 512 cm^3, respectively, yielding an equivalent diameter d_{eq} of 10 cm for all shapes. This choice ensures repeatability and enables direct comparison across shapes, minimising variability and highlighting shape-dependent effects. To further reduce variability in shape parameters, the prism and slab specimens were designed with two equal sides, ensuring a consistent aspect ratio and simplifying the interpretation of shape-dependent effects. The geometrical dimensions and proportions of the tested shapes are illustrated in Fig. 6.c. The figure also includes a classification of the adopted specimens on the particle form chart proposed by Angelidakis et al.,[67] which provides a shape-based framework that may support the generalisation of the experimental findings to other block geometries with similar aspect ratios Fig. 6.b.

3.2.1. Dynamic tests

A total of 112 drop tests were performed across the three specimen shapes. The impact velocities were controlled by varying the release height of the vacuum-based drop mechanism. Initially, a single velocity was intended for all shapes to enable direct comparison across different impact orientations and with previous results on spherical specimens. Based on the findings of Guccione et al.,[15] who reported that 10 cm mortar spheres exhibit probabilities of not fragmenting equal to 100% at velocities ≤5 m/s, 50% at 6 m/s, and 0% at higher velocities, an initial velocity of 7 m/s was selected to promote fragmentation while maintaining comparability. However, during testing, it was observed that this velocity was insufficient to induce fragmentation in cubes. As a result, the velocity for cube specimens was iteratively increased to ensure the occurrence of breakage events. Ultimately, 40 tests were conducted on cubes at three different velocities: 11 at 7 m/s (corresponding to a drop height of 2.49 m), 15 at 8 m/s (3.26 m), and 14 at 10 m/s (5.10 m). For prisms and slabs, 36 tests were performed for each shape at the original velocity of 7 m/s. The number of tests per configuration was also informed by the same study, which showed that approximately 10 repetitions are sufficient for the probabilities of not fragmenting to stabilise in spheres of this size. This benchmark was used to guide the minimum number of tests required for each velocity and shape, ensuring statistical reliability while maintaining experimental feasibility.

Table 2
Summary of test parameters. "Imp. loc." denotes the impact location: V = vertex, E = edge (with s = short, l = long), and F = face.

	Prism				Slab			
v_i	7 m/s				7 m/s			
Imp. loc.	V	E (s)	E (l)	F	V	E (s)	E (l)	F
n° (–)	31	5	–	–	29	2	4	1
Tot. n° (–)	36				36			

Cube									
v_i	7 m/s			8 m/s			10 m/s		
Imp. loc.	V	E	F	V	E	F	V	E	F
n° (–)	7	4	–	11	4	–	10	4	–
Tot. n° (–)	11			15			14		

Table 3
Percentage of fragmentation modes, specimen geometry (prism, slab, and cube). Fragmentation modes include chipping, single, and multiple fractures. Percentages should be considered per column, i.e., for equal impact velocity and impact location (Imp. loc.), or for equal velocity only ('Tot.'). V = vertex, E = edge (with s = short, l = long), and F = face.

	Prism				Slab			
v_i	7 m/s				7 m/s			
Imp. loc.	V	E (s)	E (l)	F	V	E (s)	E (l)	F
Chipping (%)	55	20	–	–	59	100	100	–
Single (%)	29	40	–	–	8	–	–	–
Multiple (%)	16	40	–	–	33	–	–	100
Tot. chip. (%)	50				66			
Tot. single (%)	31				5			
Tot. mult. (%)	19				28			

Cube									
v_i	7 m/s			8 m/s			10 m/s		
Imp. loc.	V	E	F	V	E	F	V	E	F
Chipping (%)	100	100	–	100	100	–	95	67	–
Single (%)	–	–	–	–	–	–	5	33	–
Multiple (%)	–	–	–	–	–	–	–	–	–
Tot. chip. (%)	100			100			71		
Tot. single (%)	–			–			29		
Tot. mult. (%)	–			–			–		

Impact orientation and contact location (i.e., face, edge, or vertex) were systematically varied to explore a broad range of impact scenarios. Despite efforts to randomise initial orientations, vertex impacts occurred more frequently than expected. The cause of this bias remains unclear; however it may be attributed to subtle asymmetries in specimen geometry, release alignment, or the dynamics of free fall.[11,25,26,35] Table 2 reports the investigated velocities and number of samples.

3.2.2. Static tests

A total of 60 static tests were conducted on mortar specimens of three geometries: cubes, prisms, and slabs. Two loading configurations were adopted: (i) edge-to-edge (diagonal splitting) and (ii) vertex-to-vertex (point-load-like). For cubic specimens, 10 tests were performed for each configuration. For prisms and slabs, the edge-to-edge configuration was applied in two orientations, i.e., along the short side and along the long side, with 8 tests conducted for each orientation. Additionally, 8 vertex-to-vertex tests were performed for each of these geometries. Fig. 7 illustrates all adopted configurations.

4. Results and discussion

4.1. Fragmentation

4.1.1. Dynamic loading

Drop test data were initially grouped according to the impact location: vertex, edge, or face. Three distinct outcomes were observed: (i) no fragmentation, but with localised damage at the impacted vertex, edge, or face, referred to as "chipping". This case is defined as the detachment of small fragments up to 0.5% of the initial mass from the impacted region, reflecting localised stress concentration and minor failure; (ii) fragmentation into two main parts, defined as "single fragmentation"; (iii) fragmentation into multiple pieces, referred to as "multiple fragmentation". In both fragmentation cases, chipping was also present, indicating that localised damage precedes or accompanies full breakage. For each specimen shape and impact location, Table 3 reports the percentages of occurrence for the three outcomes. For prismatic and slab-like specimens, edge impacts are further distinguished between short and long edges to account for the elongated geometry.

Across all configurations, chipping was the most prevalent outcome, particularly for cubic specimens. Fragmentation, in fact, occurred in approximately 50% of prismatic specimens and 33% of slab-like specimens, while for cubes, fragmentation was only recorded at higher velocities, with 29% of specimens fragmenting at 10 m/s, mainly under edge impact conditions. Prismatic specimens showed a more variable response. Under vertex impacts, 55% of the samples exhibited chipping, while the remaining 45% fragmented. In contrast, edge impacts (short edge only) resulted in fragmentation in 80% of the cases, indicating a lower resistance to failure along this axis. Slab-like specimens displayed similar trends under vertex impacts, as 59% of the samples chipped without fragmenting. Edge impacts, regardless of orientation, instead, resulted exclusively in chipping, suggesting that slabs are more resilient to edge impacts. These results suggest the influence of geometry and impact energy on fragmentation thresholds, indicating a higher fragmentation threshold for cubes, likely due to their symmetric geometry and uniform stress distribution.

Fragmentation in prismatic specimens typically occurs at the second contact rather than the first (Fig. 8.a1, a2), within the duration of the first impact event t_I as defined in Section 2.2.1 (Fig. 4). A similar behaviour is observed for slab specimens (Fig. 8.b1, b2), except in cases of face impact (Fig. 8.c) where fragmentation may initiate at the first contact. For cubic specimens, fragmentation, when it occurs, is typically aligned with the loading axis, i.e. normal to the impacted surface and intersecting the contact point, suggesting a more direct and symmetric failure mechanism (Fig. 8.d). The fracture pattern confirms the observed diagonal primary fractures and occasional secondary planes observed for rock specimens under edge impacts.[30] In addition, cubes exhibited fewer fracture occurrences compared to slabs and prisms, highlighting their higher resistance to dynamic failure, which is consistent with their greater compactness as illustrated in the particle form chart (Fig. 6.b).

In addition to impact location, the orientation of the specimen at impact was analysed to investigate its correlation with fragmentation occurrence and type. Ternary plots represent the angular configuration between each of the three orthogonal planes converging at the impact point, as reported in Section 2.2.1. The sum of the three angles is geometrically constrained to 180°. Separate plots are shown for prism, slab, and cube specimens (Fig. 9). For prismatic specimens, particular attention was given to the angle θ_{ABC-z}, which corresponds to the angle between the smallest square face and the impacted surface (Fig. 3). No fragmentation was observed for $\theta_{ABC-z} \leq 40°$, indicating that when the longest face is nearly vertical, the specimen tends to resist breakage. Slab specimens exhibited an even clearer trend. When $\theta_{ACD-z} < 45°$, i.e., the angle between the largest face and the impacted surface, multiple fragmentation was consistently observed. At $\theta_{ACD-z} \approx 50°$, single fragmentation occurred, while for $\theta_{ACD-z} > 60°$, only chipping was recorded. This suggests that the more the largest face impacts parallel to the target surface, the greater the likelihood of fragmentation. For cube specimens, where all faces are geometrically identical, the angles were labelled as θ_m, θ_i, and θ_M, denoting the minimum, intermediate, and maximum values, respectively. Fragmentation was observed when

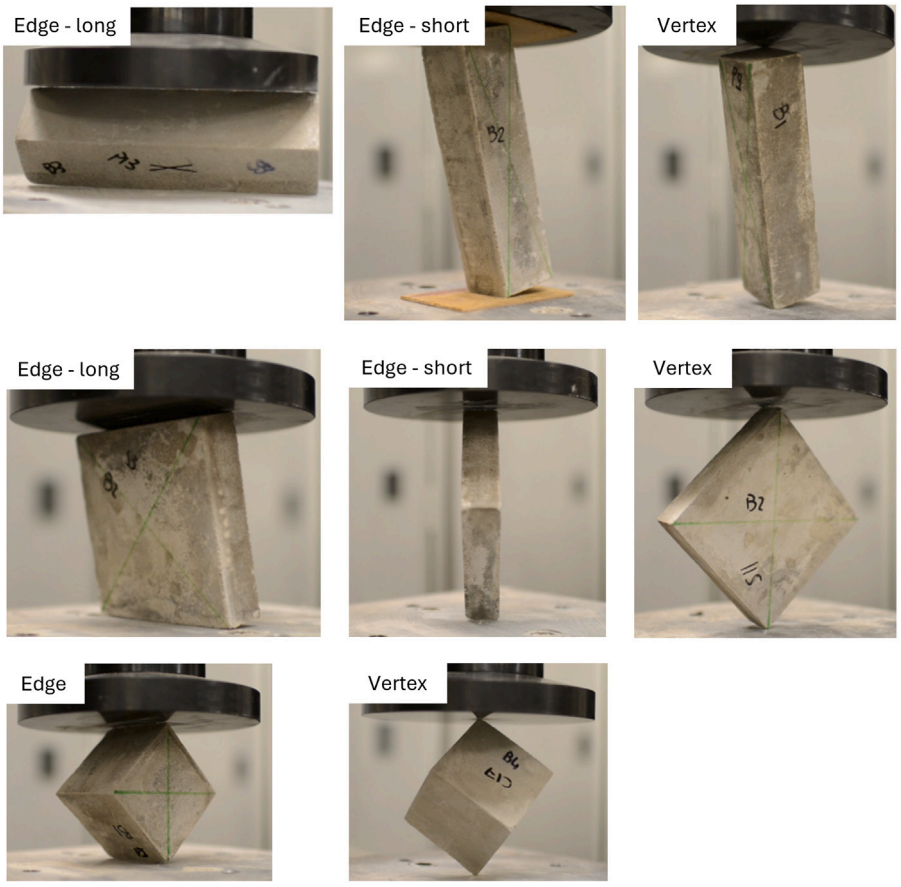

Fig. 7. Static test setups illustrating edge-to-edge and vertex-to-vertex loading conditions across different specimen geometries (prisms, slabs, cubes).

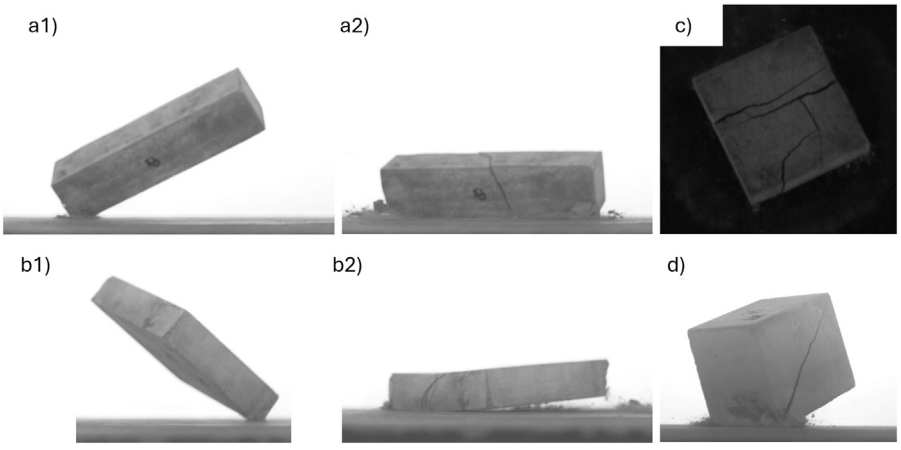

Fig. 8. Impact and fragmentation sequences for different specimen shapes and contact configurations. (a1) Vertex impact with single fragmentation occurring at the second contact (prism); (a2) corresponding fragmentation event. (b1) Vertex impact with fragmentation at the second contact (slab); (b2) corresponding fragmentation event. (c) Face impact on a slab specimen. (d) Edge impact on a cube specimen with single fragmentation. All images are shown in side view, except for (b), which is presented in plan view.

one face was nearly normal to the impacted surface, i.e., typically corresponding to an impact location on the edge. Results from slab and prism specimens suggest that fragmentation is more prone to occur when the shortest side is aligned with the loading axis. This configuration appears to promote stress concentration and reduce the ability of the specimen to redistribute impact forces, thereby increasing the likelihood of breakage.

To complement the orientation analysis, the effect of the normalised impact eccentricity d/d_{eq}, defined as the horizontal distance between the impact point A and the projection of the specimen's centre of gravity (CoG) onto the impact plane, normalised by the diameter of a sphere with equivalent volume d_{eq}, was investigated (Fig. 10). Prismatic specimens display a wider range of d/d_{eq} values, attributed to their elongated geometry, which allows for greater variability in impact configurations. It was observed that fragmentation becomes increasingly likely as d/d_{eq} increases, consistent with trends identified through orientation analysis. Specimens impacted closer to their CoG tended to rebound or chip without fragmenting, whereas those with larger

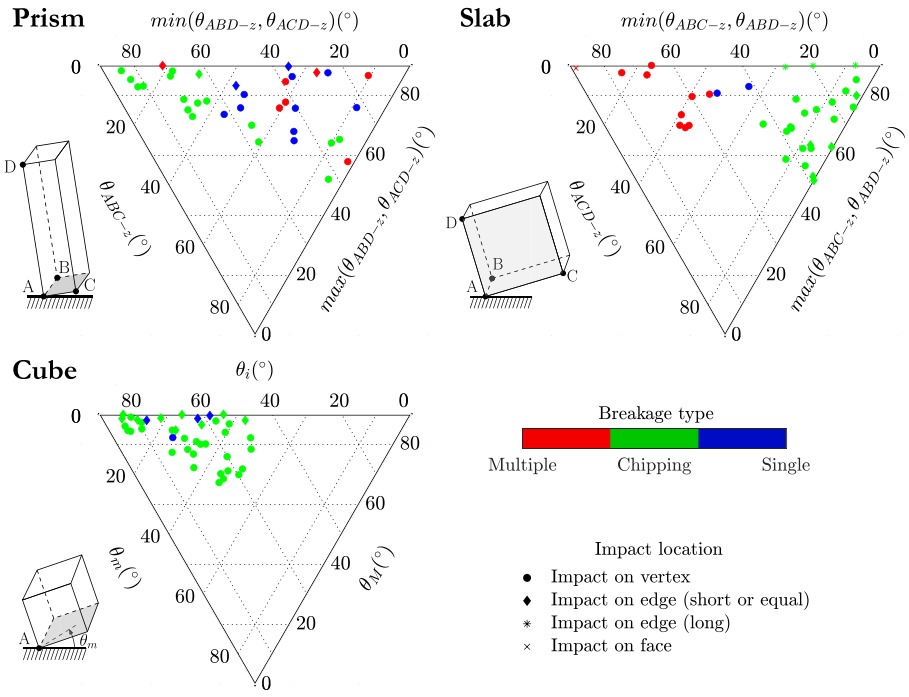

Fig. 9. Ternary plots of the angles between each of the three orthogonal planes, *A–B–C*, *A-B-D*, and *A-C-D* and the impacted surface, corresponding to the angles θ_{ABC-z}, θ_{ABD-z}, and θ_{ACD-z}, respectively. Separate plots are shown for prism, slab, and cube specimens. For cube specimens, where the faces are equal, the subscripts *m*, *i*, and *M* denote the minimum, intermediate, and maximum θ angles, respectively. Symbols indicate the impact location: circles for vertex impacts, diamonds and stars for edge impacts, and crosses for face impacts.

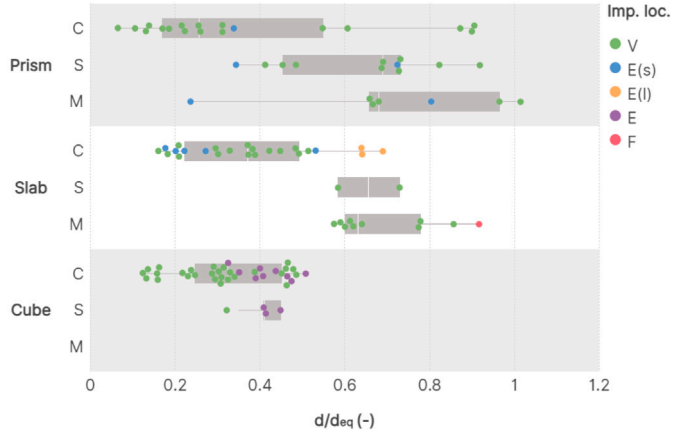

Fig. 10. Boxplot of the normalised impact eccentricity d/d_{eq}. The data are subdivided by specimen shape (cubes, prisms, slabs) and grouped by fragmentation mode (C = chipping, i.e., no clear fragmentation, S = single, M = multiple fragmentation) to highlight the influence of impact eccentricity on breakage severity. Each test is colour-coded according to impact location: vertex (V), edge (E), or face (F).

normalised eccentricities exhibited higher fragmentation rates. This suggests that eccentric impacts, often with the shortest side aligned to the loading axis, promote stress concentrations and bending (flexural) stresses, increasing the likelihood of fragmentation. As with previous findings, this reinforces the role of impact orientation, in conjunction with geometry, contact location, and asymmetry, in governing failure mechanisms and fragmentation behaviour.

To further characterise the fragmentation behaviour, the empirical cumulative distribution function $F(x)$ was computed for fragments with mass $m_f \geq 1\%$ of the initial specimen mass m_i (Fig. 11.a). This threshold was selected to exclude small chips, which were present

Table 4
Number of fragments (n_f) with $m_f \geq 10\%$ m_i for multiple fragmentation cases.

Shape	Minimum	Median	Maximum
Prism	3	3	5
Slab	3	5	8

in all tests and do not reflect significant breakage. As fragmentation in cubes was limited to four cases of single fracture, only prism and slab specimens were included in this analysis. For each geometry, the cumulative distribution was constructed by analysing the fragments of all the tests, without averaging across specimens. This approach provides a representative view of the overall fragmentation severity and mass distribution, preserving the variability in fragment number and size inherent to each impact event, which is particularly relevant given the limited sample size and the stochastic nature of fragmentation.

The results reveal distinct trends. For prismatic specimens, fragmentation typically involved a single fracture dividing the specimen approximately in half. Accordingly, the 95th percentile of $F(x)$ corresponds to fragments retaining about 65% of the initial mass. In contrast, slab specimens exhibited more extensive fragmentation, with smaller fragments dominating the mass distribution. For slabs, the 80th percentile of $F(x)$ falls below 30% of the initial mass, indicating a higher degree of fragmentation and finer fragment sizes. To complement this analysis, the number of fragments with mass m_f larger than 10% m_i was recorded for cases classified as multiple fragmentation (Table 4). The data shows differences in fragmentation severity between shapes. Slabs consistently produced a greater number of substantial fragments, while prisms tended to yield fewer, larger pieces.

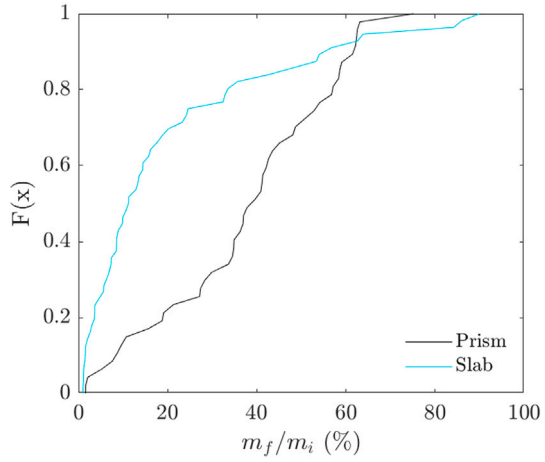

Fig. 11. Empirical cumulative distribution function $F(x)$ of fragment masses $m_f \geq 1\%$ of the initial specimen mass m_i, excluding small chips.

Table 5
Percentage of observed fracture modes, categorised by test type (edge-to-edge and vertex-to-vertex) and specimen geometry (prisms, slabs, and cubes). The fracture modes include Tensile Splitting Fracture (TSF), Tensile Splitting Fracture with secondary Partitioning (TSF+P), and Delamination Fracture (DF).

Prism			
Test	Edge-to-edge (long)	Edge-to-edge (short)	Vertex-to-vertex
TSF (%)	38	–	–
TSF+P (%)	62	–	–
DF (%)	–	100	100
Slab			
Test	Edge-to-edge (long)	Edge-to-edge (short)	Vertex-to-vertex
TSF (%)	–	38	38
TSF+P (%)	–	–	–
DF (%)	100	62	62
Cube			
Test	Edge-to-edge		Vertex-to-vertex
TSF (%)	90		90
TSF+P (%)	10		–
DF (%)	–		10

4.1.2. Static loading

Three distinct fracture modes were identified in both edge-to-edge splitting and vertex-to-vertex tests conducted on mortar specimens: Tensile Splitting Fracture (TSF), Tensile Splitting Fracture with a secondary Partitioning (TSF+P), and Delamination Fracture (DF). Table 5 presents the percentage of the observed fracture modes. TSF corresponds to the classical diametral rupture along the loading axis and was predominantly observed in cubes (all loading cases, Fig. 12.a and .b) and prismatic specimens subjected to edge-to-edge loading involving the long edge (Fig. 12.c). In 62.5% of these cases, the primary diametral fracture was accompanied by a secondary partitioning (TSF+P), characterised by the formation of an additional crack plane approximately parallel to the smallest face of the specimen. This secondary fracture typically developed orthogonally to the main rupture and effectively divided the specimen into two halves along its shortest dimension (Fig. 12.d). TSF was also observed in 37.5% of slab tests under both vertex-to-vertex (Fig. 12.g) and short-edge configurations (Fig. 12.h). For slabs, TSF label was retained even when no clear diametral failure occurred, as the fracture direction slightly deviated from the ideal diametral axis, occasionally promoting secondary branches (Fig. 12.h).

Delamination Fracture (DF), defined by surficial damage and progressive flaking, was observed in both edge-to-edge (Fig. 12.e and .i) and vertex-to-vertex tests (Fig. 12.j). This mode arises when asymmetrical chipping or flaking occurs, despite the contact points (edges or vertices) being vertically aligned during setup. The origin of this asymmetry is attributed to (i) inherent imperfections in the specimens and (ii) increased difficulty in accurately positioning taller specimens.

The analysis of the load–displacement curves revealed distinct trends associated with each fracture mode. Fig. 13 presents representative curves for all observed fracture types, organised by specimen geometry (cubes, prisms, slabs) and loading configuration, edge-to-edge (long and short) and vertex-to-vertex. Fracture modes are colour-coded: green for Tensile Splitting Fracture (TSF), blue for TSF with secondary partitioning (TSF+P), and red for Delamination Fracture (DF).

In edge-to-edge splitting tests, specimens exhibiting TSF behaviour showed a well-defined linear elastic region followed by an abrupt load drop at peak force, indicative of sudden diametral rupture. In contrast, TSF+P cases were characterised by multiple distinct peaks. While prismatic specimens typically displayed two peaks, i.e., one associated with the formation of a secondary rupture plane parallel to the shortest face and a second corresponding to the final diametral fracture, the unique cubic specimen displaying TSF+P behaviour showed more than two peaks, reflecting sequential crack development across multiple planes.

Specimens exhibiting DF showed markedly different mechanical behaviour (see red curves in Fig. 13), with progressive damage accumulation and localised sliding indicative of inelastic deformation mechanisms preceding failure. The absence of a sharp load drop reflects the influence of surface flaking, frictional resistance, and asymmetric stress redistribution. Similar trends were observed in vertex-to-vertex tests, where TSF cases retained a linear elastic region, often accompanied by minor oscillations prior to peak load. These fluctuations are attributed to localised chipping at the contact points, which influence crack initiation.

Looking to symmetry of crack propagation, in the cases involving TSF (with or without secondary partitioning) the primary fracture developed along the loading axis, confirming the tensile nature of its tensile failure. The crack remained close to vertical and facilitated the identification of the fracture plane. Accordingly, tests classified as TSF or TSF+P were considered for quantitative analysis of tensile resistance, while fractures involving delamination or irregular mechanisms were excluded due to their progressive and non-localised failure behaviour. For edge-to-edge configurations, the equivalent splitting tensile strength was evaluated according to Eq. (5). Owing to the generally symmetric nature of TSF cracks, the area of the fracture plane A_p was defined as the vertical cross-sectional area between the two loaded edges, corresponding to the plane along which the primary tensile fracture developed. Table 6 displays the minimum, median and maximum values of equivalent splitting tensile strength for each specimen geometry. Prismatic specimens show the highest median value (2.34 MPa), followed by cubes (1.83 MPa). The three slab specimens yield values clustered around 1.1 MPa, indicating lower and more consistent strength across tests. These values appear consistent with the average tensile strength obtained from Brazilian Tests (2.05 MPa), although the observed variability highlights the influence of specimen geometry, loading configuration, and contact conditions on the fracture response.

For vertex-to-vertex tests involving TSF, tensile strength was evaluated using Eq. (6). Table 7 reports the minimum, median and maximum values of the estimated tensile strength for each specimen geometry. Cube specimens show a median tensile strength of 0.58 MPa, while slab specimens display consistent results with a median of 0.16 MPa. Prisms are not represented, as they exhibited only DF-type failures and were therefore excluded from this subset of tests. Based on these results, an empirical conversion factor of approximately 0.27, defined as the ratio between the median tensile strength of slabs and cubes, Eq. (6), can be used to relate tensile strength values across these two geometries.

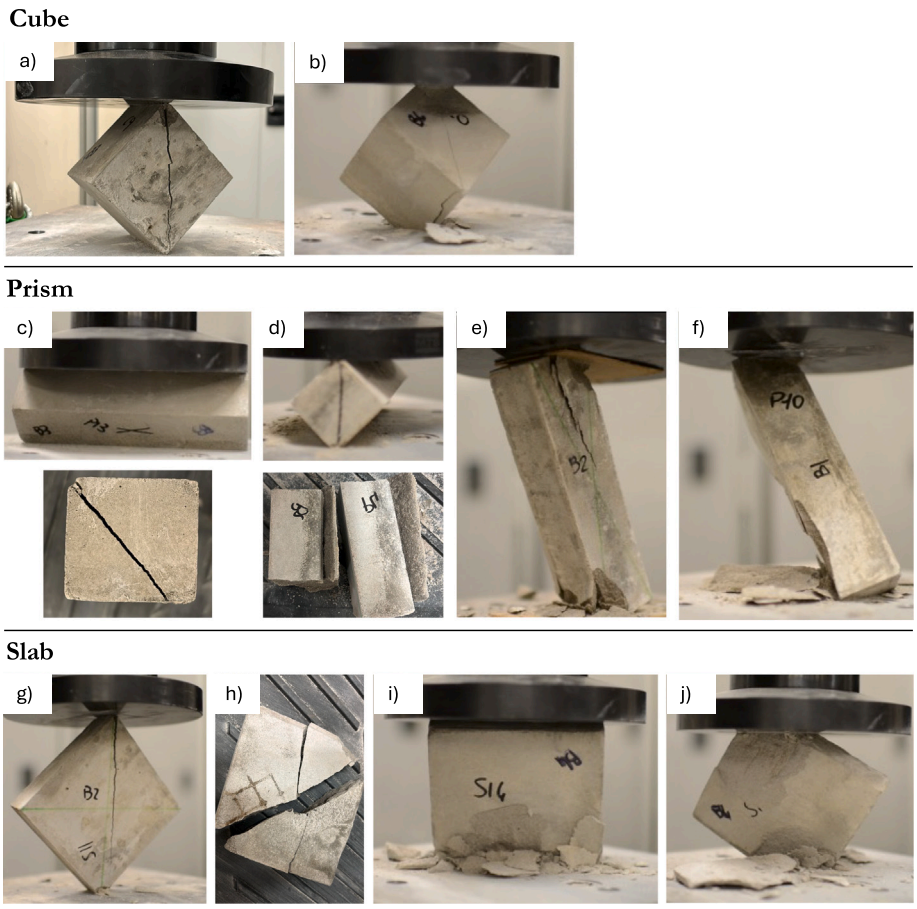

Fig. 12. Final stage of static splitting tests on cubic (a, b), prism-like (c–f), and slab-like (g–l) specimens. For the cubes, test (a) corresponds to edge-to-edge loading, while (b) shows the vertex-to-vertex configuration; both exhibit a TSF fracture mode. For the prisms, tests (c) and (d) were conducted under edge-to-edge loading along the long side, with (c) showing a TSF and (d) a TSF+P fracture mode. Specimen (e) was tested along the short side and displays a DF fracture mode, while (f) corresponds to the vertex-to-vertex configuration, also showing DF. For the slabs, test (g) corresponds to the vertex-to-vertex configuration with a TSF fracture mode. Tests (h) and (l) were both conducted under edge-to-edge loading along the short side, while (i) was tested along the long side; (h) shows TSF, whereas (i) and (j) display DF fracture modes.

Table 6
Equivalent splitting tensile strength, calculated by dividing the peak force (F_p) by the area of the fracture plane (A_p), for edge-to-edge loading (TSF and TSF+P cases). For prisms, only the long edge-to-edge configuration is considered, and for slabs, only the short edge-to-edge configuration, as these displayed TSF and TSF+P failure modes.

Shape	Minimum (MPa)	Median (MPa)	Maximum (MPa)
Prism	1.62	2.34	2.75
Cube	1.17	1.81	2.89
Slab	1.04	1.13	1.23

Table 7
Approximate tensile strength for vertex-to-vertex loading (TSF and TSF+P cases), computed as $0.9F_p/D^2$, where D is the distance between the loading points. Prism specimens are excluded due to the absence of TSF-type failures under vertex-to-vertex loading.

Shape	Minimum (MPa)	Median (MPa)	Maximum (MPa)
Cube	0.41	0.58	0.69
Slab	0.13	0.16	0.17

While not being a general shape-dependent correction factor like the one proposed by Broch and Franklin,[64] this empirical ratio may serve as a preliminary reference for comparing vertex-to-vertex tensile strength between slab-like and cubic specimens.

4.1.3. Linking static to dynamic behaviour

The static splitting tests, conducted under both edge-to-edge and vertex-to-vertex configurations, provide valuable context for interpreting the dynamic fragmentation behaviour observed in drop tests. Despite the different loading conditions, both configurations revealed geometry-dependent fracture mechanisms that align with the dynamic response of the specimens.

Cubic specimens consistently exhibited TSF fracture modes in static tests, with relatively high tensile strength values under both configurations. This correlates with their robustness, both under edge and vertex impacts. The uniform geometry of cubes promotes balanced stress distribution and predictable crack propagation, contributing to their higher resistance to dynamic failure.

Slabs, in contrast, showed lower tensile strength and a higher incidence of delamination fractures (DF), especially under long-edge and vertex loading. These static observations mirror the dynamic results, where slabs were more prone to fragmentation under vertex impacts compared to cubes. The thin geometry of slabs appears to reduce their capacity to accommodate impact forces, making them more prone to localised failure when impacted at corners.

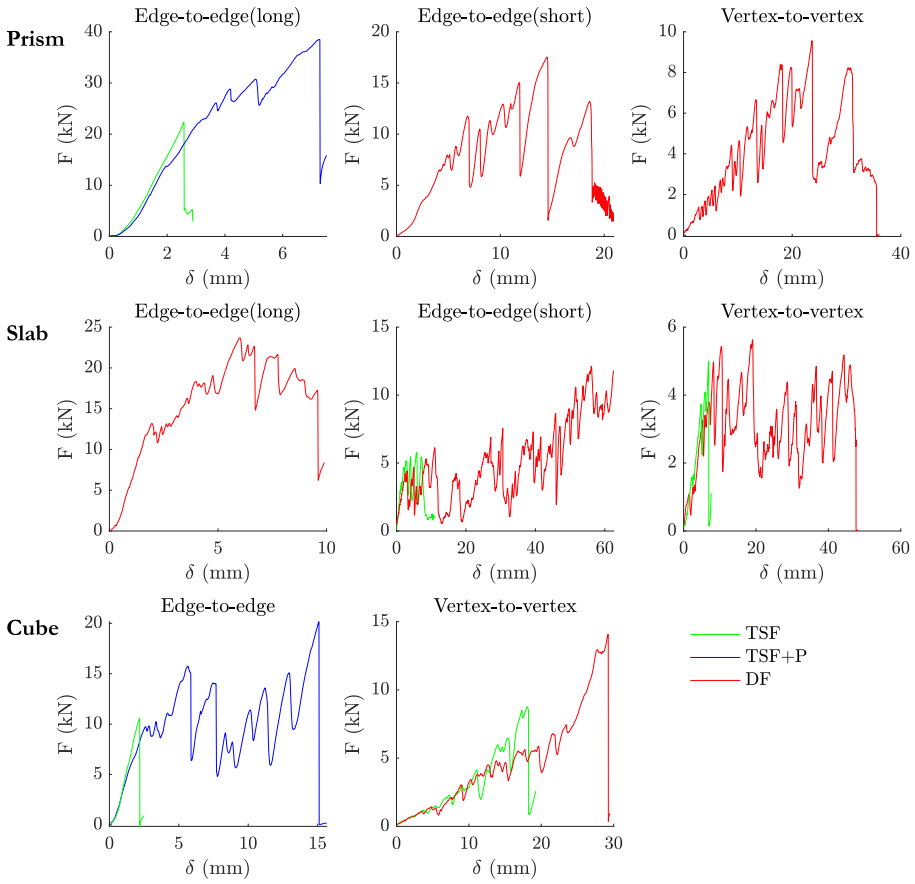

Fig. 13. Representative load–displacement curves for each observed fracture mode, grouped by specimen geometry (cubes, prisms, slabs) and loading configuration: edge-to-edge (long and short) and vertex-to-vertex. Curves corresponding to Tensile Splitting Fracture (TSF) are shown in green, TSF with secondary partitioning (TSF+P) in blue, and Delamination Fracture (DF) in red.

Despite prismatic specimens displaying the highest tensile strength under long-edge static loading, their dynamic response revealed a greater propensity for fragmentation when the impact was aligned with the shortest axis. Nevertheless, in the dynamic tests, no long-edge impact configurations occurred, limiting the potential for stress redistribution and making the specimens more vulnerable to failure under eccentric loading.

Overall, the static tests confirm that fracture mode and tensile strength are strongly influenced by specimen geometry and loading configuration. These factors, in turn, govern the dynamic fragmentation occurrence and failure mode. While not all static configurations are replicated under dynamic conditions, the observed fracture modes offer valuable qualitative insight into the geometric toughness of the specimens. In static splitting tests, the loading axis is deliberately aligned with the specimen's centre of gravity (CoG), allowing controlled stress application and a reasonable interpretation of fracture behaviour. In contrast, dynamic impacts involve complex, non-collinear interactions where the contact force is rarely aligned with the CoG, making it difficult to replicate the same loading conditions. This discrepancy prevents a direct comparison between the energy required to induce failure in static and dynamic cases. For spherical specimens, such comparison is feasible due to the inherent collinearity of impact and symmetry of stress distribution. For angular blocks, however, the variability in contact configuration and induced moments necessitated thus the adoption of a shape-aligned local reference system to evaluate post-impact motion. Despite these limitations, the findings highlight the value of static mechanical characterisation in informing predictive models of rockfall behaviour, particularly for identifying shape-dependent fragility and potential energy dissipation mechanisms.

4.2. Energy dissipation and rebound dynamics

This subsection focuses on energy dissipation in specimens exhibiting only chipping. These tests provide a controlled framework for analysing rebound behaviour and energy loss mechanisms without the complexity introduced by fragments motion. Table 8 provides an overview of the post-impact outcomes observed across all tests, including fragmentation, sliding, bouncing, and resting behaviours. "Out of record" cases refer to tests where the impact duration t_I could not be fully captured within the recorded image sequence due to camera limitations. In cases where fragmentation did not occur, bouncing was the predominant post-impact behaviour.

4.2.1. Impact duration and multi-contact interactions

Impact duration t_I, defined as the time during which the specimen's centre of gravity remains at or below its position from the preceding instant (without sliding or coming to rest) was measured by images analysis. Due to the frame rate of the cameras (500 fps), the temporal resolution is limited to 0.002 s. Within this interval, the number of distinct contacts n_c was manually counted through frame-by-frame analysis. Fig. 14 presents a scatter plot of t_I versus n_c, with data colour-coded by specimen shape. Prismatic specimens generally exhibit $n_c \leq 5$, with both median and mean values equal to 4. The corresponding impact duration is approximately 0.16 s. Slab specimens show a broader range of contact counts, with n_c reaching up to 8, yet maintain a shorter median t_I of 0.04 s but a higher mean of 0.18 s. Cubic specimens display the shortest impact durations, consistently below 0.06 s, and a maximum of three contact events, with a median n_c of 2. Across all specimen shapes, longer impact durations tend to be

Table 8
Percentage of post-impact outcomes for all tested specimens: fragmentation, sliding, bouncing, and resting. Results are grouped by specimen shape. 'OoR' stands for "Out of record", which refers to tests where the impact duration t_I could not be fully captured within the recorded image sequence due to camera limitations. Percentages should be considered per column, i.e., for equal impact velocity and impact location (Imp. loc.), or for equal velocity only ('Tot.'). V = vertex, E = edge (with s = short, l = long), and F = face.

	Prism				Slab			
v_i	7 m/s				7 m/s			
Imp. loc.	V	E (s)	E (l)	F	V	E (s)	E (l)	F
Bounce (%)	35	–	–	–	37	80	100	–
Slide (%)	3	–	–	–	–	–	–	–
Rest (%)	10	–	–	–	3	–	–	–
OoR (%)	7	20	–	–	19	–	20	–
Fragment (%)	45	80	–	–	41	–	–	100
Tot. bounce (%)	31				47			
Tot. slide (%)	3				–			
Tot. rest (%)	8				3			
Tot. OoR (%)	8				17			
Tot. frag. (%)	50				33			

Cube									
v_i	7 m/s			8 m/s			10 m/s		
Imp. loc.	V	E	F	V	E	F	V	E	F
Bounce (%)	88	100	–	100	100	–	80	25	–
Slide (%)	–	–	–	–	–	–	10	–	–
Rest (%)	12	–	–	–	–	–	10	–	–
OoR (%)	–	–	–	–	–	–	–	–	–
Fragment (%)	–	–	–	–	–	–	–	75	–
Tot. bounce (%)	91			100			64		
Tot. slide (%)	–			–			29		
Tot. rest (%)	9			–			–		
Tot. OoR (%)	–			–			–		
Tot. fragm. (%)	–			–			29		

associated with a greater number of contact events. This observation reflects the increased complexity of contact interactions in specimens with angular or elongated geometries, which often experience multiple sequential impacts during rebound.

It is important to note that the number of contacts and the dynamics within a single impact event are highly complex and depend strongly on the impact location, orientation, and the position of the specimen's centre of gravity. As highlighted by high-speed image sequences, intricate combinations of rotation and translation can occur within a single t_I, especially in specimens with elongated or asymmetric geometries, i.e., prisms and slabs. As an example, Figs. 15 and 16 illustrate two representative contact sequences for prism and slab specimens, respectively. For both shapes, the first sequences (Figs. 15.a and 16.a) display a short impact duration with only two distinct contact events. In contrast, the second sequences (Figs. 15.b and 16.b) show specimens undergoing a prolonged impact phase characterised by multiple contacts and complex motion, including rotation, within t_I. These examples highlight the variability in contact dynamics and the influence of specimen geometry on energy dissipation mechanisms. Despite not analysed specifically, it is also worth noting that, as highlighted in Section 4.1.1, in cases where fragmentation occurred, both t_I and n_c were significantly reduced.

4.2.2. Post-impact trajectory and rebound analysis

Post-impact motion was analysed to understand rebound behaviour and energy partitioning. Velocity components immediately after t_I were tracked in the local reference system (ξ, η, z), previously defined with respect to the specimen geometry.

A total of 56 drop tests were tracked: 9 for prismatic specimens, 16 for slab-like specimens, and 31 for cubes. For the latter, 10 tests were conducted at 7 m/s, 14 at 8 m/s, and 7 at 10 m/s. For simplicity, the translational velocity of the centre of gravity immediately after impact is denoted as v_e, with components v_ξ, v_η, and v_z reported without the subscript.

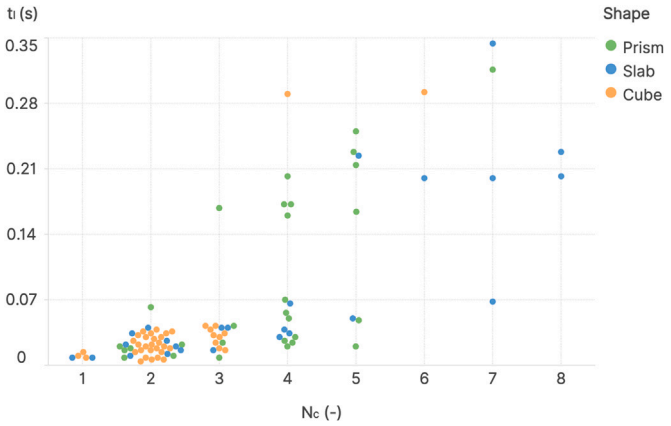

Fig. 14. Scatter plot of impact duration t_I versus number of contact events n_c, colour-coded by specimen shape (cubes, prisms, slabs). An increasing trend is observed between t_I and n_c across all specimen shapes.

Figs. 17, 18, and 19 illustrate the post-impact velocity vectors of the specimens in the ξ–η, ξ–z, and η–z planes for prismatic, slab-like, and cubic geometries, respectively. The post-impact velocity vector, v_e, was estimated by resolving its components along the ξ, η, and z directions, i.e., v_ξ, v_η, and v_z, as detailed in Section 2.2.1. Table 9 summarises the maximum and minimum (including maximum in the negative direction) values of the velocity components observed for each shape and impact velocity v_i. Fig. 20 presents the rebound angles β and α plotted against a representative impact orientation angle for each specimen shape. In line with the approach used to analyse fragmentation occurrence, the selected orientation angles are: θ_{ABC-z} for prismatic specimens (angle between the smallest square face and the impacted surface), θ_{ACD-z} for slabs (angle between the largest face and the impacted surface), and θ_m for cubes (minimum angle among the three orthogonal faces and the impacted surface). The angle β describes the horizontal rebound direction, measured clockwise from the η-axis to the velocity vector projected onto the impacted surface, i.e., the ξ–η plane. The angle α quantifies the vertical component of rebound motion, defined between the vertical velocity and the horizontal velocity magnitude in the ξ–η plane.

For all shapes, with few exceptions (one for prisms, two for slabs, and three for cubes), the post-impact motion is directed along the positive ξ axis, i.e., from the impact point towards the centre of gravity.

Prismatic specimens exhibit a wide range of rebound trajectories in the horizontal direction, i.e., parallel to the impacted surface. This is reflected in the distribution of the angle β, which reaches up to 190°, indicating significant lateral scattering. All velocity components remain below (approximately) 1 m/s, with v_ξ generally showing the lowest values. Among the tested impact configurations, only vertex impacts consistently result in bouncing behaviour, making them the only cases where post-impact motion could be reliably tracked. No clear trend was observed in the vertical direction of rebound motion, as indicated by the angle α, which remained below 60° across all tests.

For slab-like specimens, rebound motion in the horizontal direction predominantly occurs along both the positive ξ and η axes. The angle β generally remains below 90° indicating a relatively stable trajectory aligned with the specimen geometry. The velocity components reach up to 1.90 m/s for v_ξ, 1.42 m/s for v_η, and 1.32 m/s for v_z. Compared to prisms, slabs remain more consistently aligned with the ξ axis, indicating a more stable rebound direction and reduced lateral scattering. Negative values of v_η (i.e., $90° < \beta < 180°$) are observed only when the largest face is more inclined relative to the impact surface ($\theta_{ACD-z} \approx 60°$), indicating that deviation from normal orientation may promote

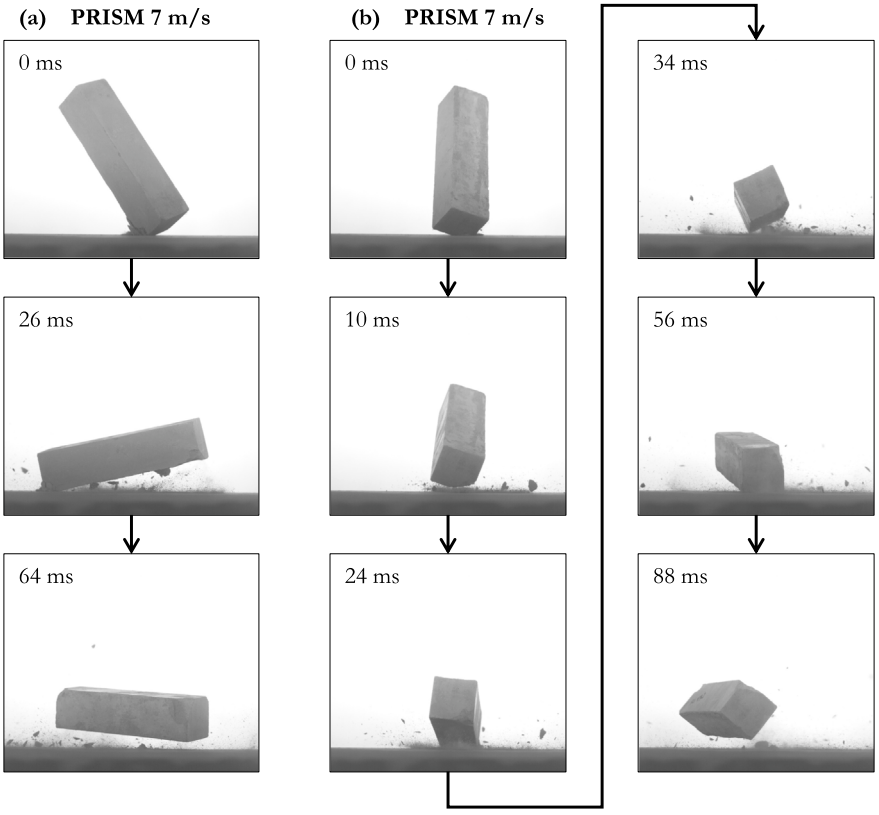

Fig. 15. Contact sequences for a prismatic specimen. (a) Short impact duration with two distinct contact events and limited rotation. (b) Prolonged impact duration with multiple contacts and complex motion.

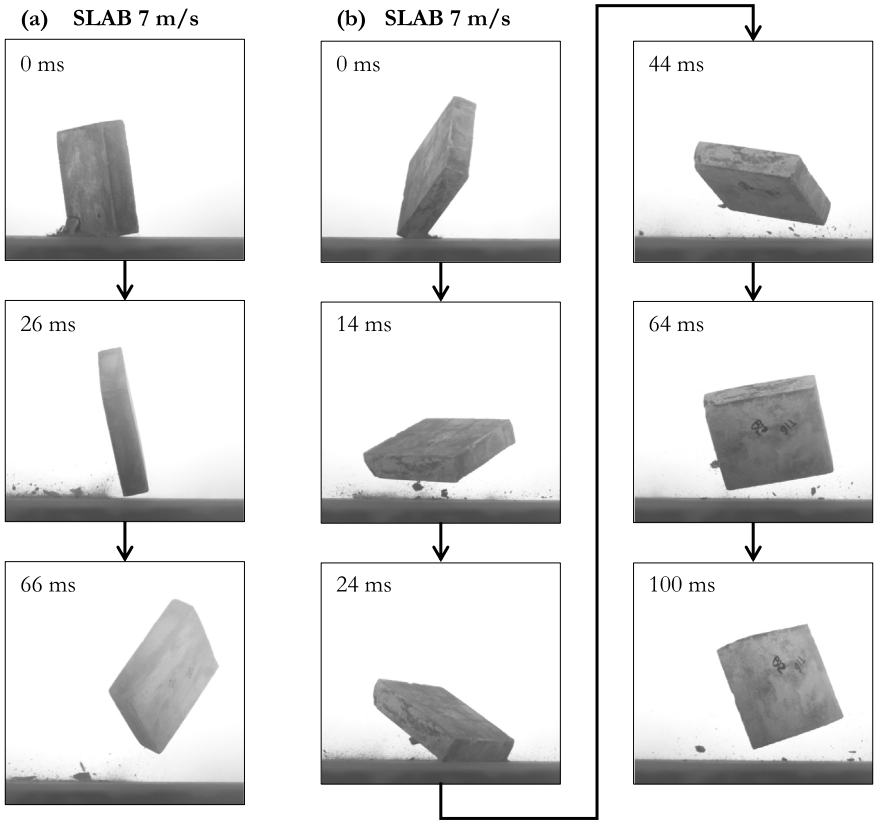

Fig. 16. Contact sequences for a slab-like specimen. (a) Short impact duration with two distinct contact events and limited rotation. (b) Prolonged impact duration with multiple contacts and complex motion.

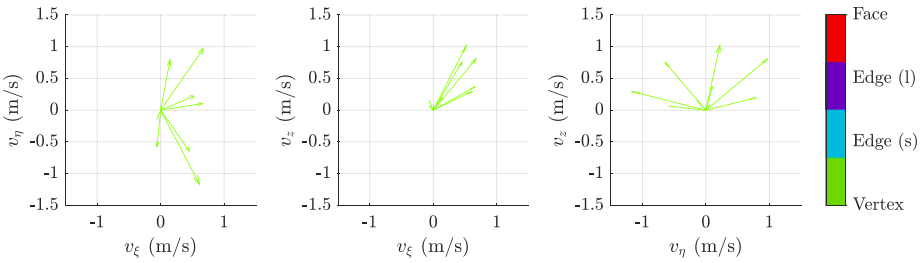

Fig. 17. Post-impact velocity vectors for the prisms, in the $\xi - z$ and $\eta - z$ planes subdivided according to impact location.

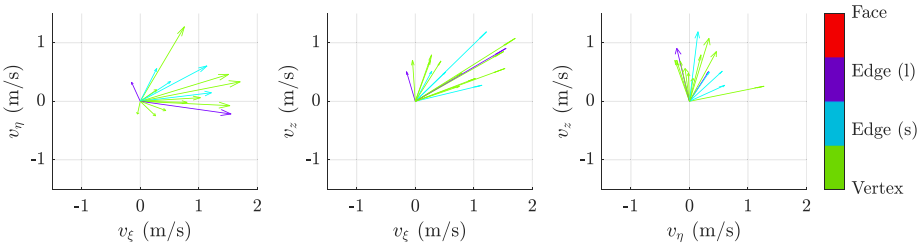

Fig. 18. Post-impact velocity vectors for the slabs, in the $\xi - z$ and $\eta - z$ planes subdivided according to impact location.

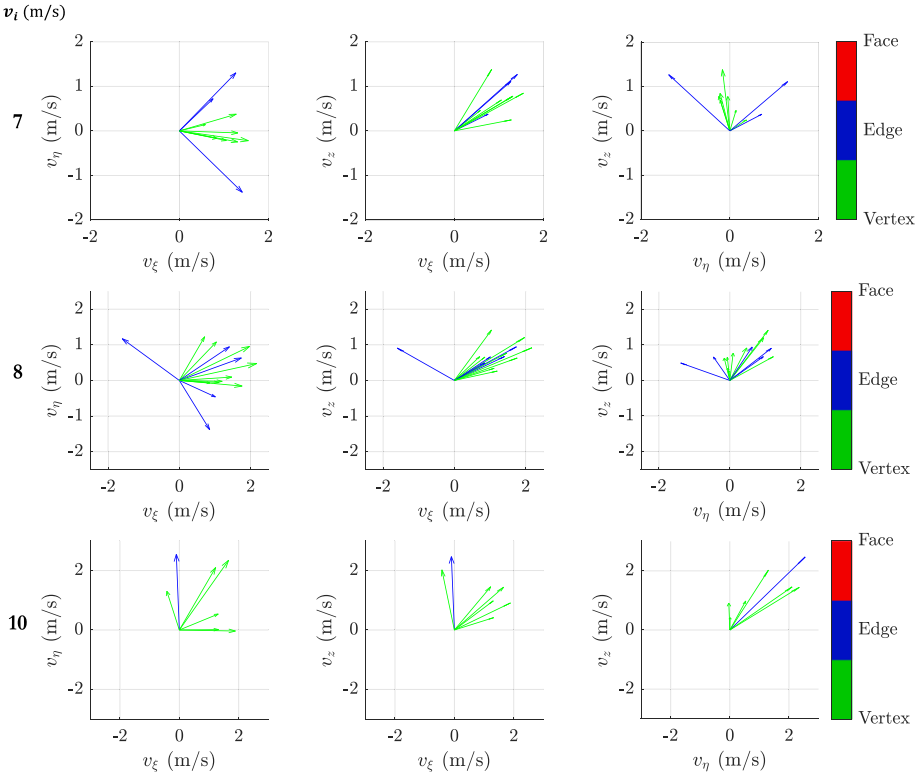

Fig. 19. Post-impact velocity vectors for the cubes, in the $\xi - z$ and $\eta - z$ planes subdivided according to impact location. Each row corresponds to an impact velocity v_i.

horizontal dispersion. A single case displays $\beta \approx 350°$, corresponding to a long-edge impact. Regarding the vertical projection angle α, a decreasing trend is observed with increasing θ_{ACD-z}, indicating that when the largest face is nearly perpendicular to the impacted surface, the rebound becomes more horizontal. The angle α reaches up to 80°, reflecting a strong vertical component.

For cube specimens at the lowest impact velocity, rebound motion shows a dependence on impact location. Vertex impacts result in trajectories predominantly aligned with the positive ξ axis, corresponding to $\beta \approx 90°$, while edge impacts produce more dispersed horizontal directions, though still generally within $\beta \leq 180°$. No consistent trend was observed with respect to impact orientation. As expected, increasing the impact velocity leads to higher post-impact velocities across all components. In terms of vertical motion, the angle α remains below 60° and shows a slight decreasing trend with increasing θ_m. This suggests that when a face is more parallel to the impacted surface, the rebound becomes increasingly horizontal.

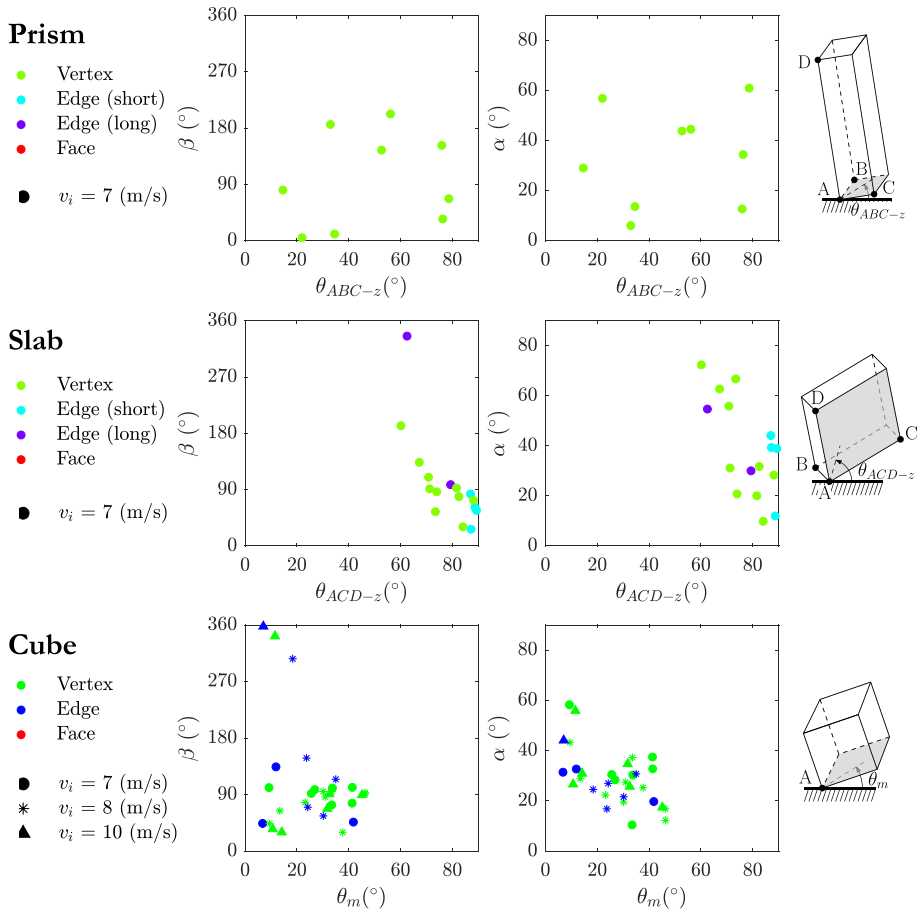

Fig. 20. Left column: planar angle β, measured clockwise from the η-axis to the velocity vector, plotted against a representative impact orientation angle: θ_{ABC-z} for prisms, θ_{ACD-z} for slabs, and θ_m for cubes. Right column: vertical projection angle α, defined between the vertical and horizontal velocity components, plotted against the same orientation angles.

Table 9
Maximum and minimum (maximum in negative direction) values of the velocity components observed in each shape for each impact velocity v_i.

	Prism		Slab	
v_i	7 m/s		7 m/s	
Axis	≥0	<0	≥0	<0
v_ξ (m/s)	0.75	0.06	1.90	0.17
v_η (m/s)	0.90	1.30	1.42	0.24
v_z (m/s)	1.14	–	1.32	–

Cube						
v_i	7 m/s		8 m/s		10 m/s	
Axis	≥0	<0	≥0	<0	≥0	<0
v_ξ (m/s)	1.72	–	2.42	1.78	2.10	0.47
v_η (m/s)	1.44	1.53	1.37	1.54	2.83	0.04
v_z (m/s)	1.54	–	1.57	–	2.75	0

4.2.3. Apparent coefficient of restitution

Fig. 21 presents the relationship between impact orientation and rebound behaviour for non-fragmented specimens. The left column shows the apparent coefficient of restitution ($|v_e/v_i|$), while the right column displays the normal restitution coefficient ($|v_z/v_i|$), both plotted against a representative orientation angle for each shape, selected as for β and α analysis. The apparent restitution coefficient remains below 0.25 for prisms, about 0.35 for slabs, and up to 0.39 for cubes, confirming the trend observed in t_I: prisms tend to have longer contact durations and higher energy dissipation. Similarly, the normal restitution coefficient $|v_z/v_i|$ is the lowest for prisms (below 0.17), followed by slabs (below 0.19), and the highest for cubes (up to 0.28), indicating that post-impact motion is predominantly tangential to the impacted surface in all cases.

For prismatic specimens, a slight increasing trend in both $|v_e/v_i|$ and $|v_z/v_i|$ is observed with increasing θ_{ABC-z}, suggesting that when the largest face is parallel to the impacted surface, energy dissipation is reduced. This behaviour is attributed to the high non-collinearity of the contact, which results in lower impact forces at the contact point. Slabs show an opposite trend with increasing θ_{ACD-z}, indicating that impacts with the largest face normal to the surface result in lower dissipation because of the number of contacts is generally limited to 2 or 3. Finally, cube specimens exhibit a strong decreasing trend in both restitution coefficients with increasing θ_m, meaning that impacts with a face parallel to the impacted surface dissipate less energy. This trend holds for both vertex and edge impacts and for all impact velocities. Observed restitution coefficient values for cubes are lower than those reported for harder rocks, consistent with Asteriou et al.[10] Although they did not report specimen orientation at impact, nor the exact impact point or number of contacts, they found mean normal restitution coefficients at 5 m/s ranging from 0.36 (marl) to 0.66 (sandstone) for cubic specimens, noting that the normal coefficient of restitution increases with material hardness. These observations are consistent with Dattola et al.,[27] who reported a strong sensitivity of the restitution coefficient to initial orientation and a decrease in restitution coefficient with increasing aspect ratio. Our results confirm these trends, with cubes consistently exhibiting higher restitution coefficients than slabs and prisms.

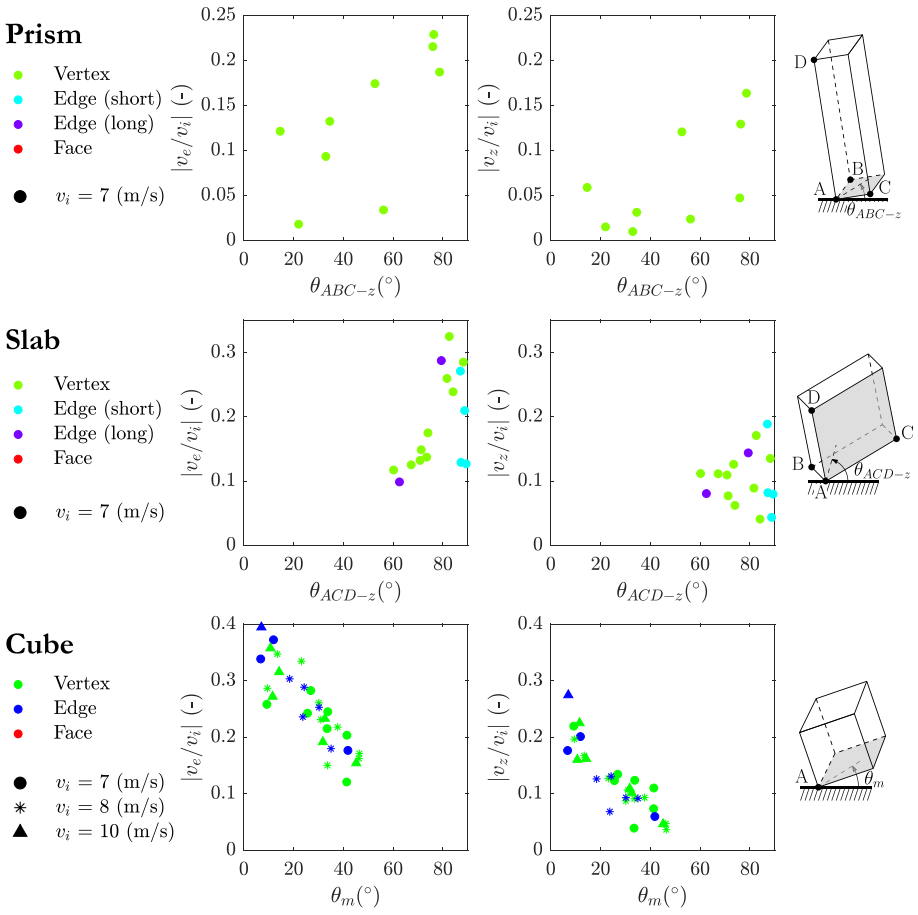

Fig. 21. Restitution analysis for non-fragmented specimens. Left column: apparent coefficient of restitution ($|v_e/v_i|$) plotted against a representative impact orientation angle, θ_{ABC-z} for prisms, θ_{ACD-z} for slabs, and θ_m for cubes. Right column: normal restitution coefficient ($|v_z/v_i|$) versus the same angles.

4.2.4. Comparison with spheres

To contextualise the rebound behaviour of angular specimens, Table 10 compares the apparent coefficient of restitution $|v_e/v_i|$ and impact duration t_I across cubes, prisms, slabs, and spherical specimens of equivalent volume and material. A visual representation of this comparison is provided in Fig. 22, which illustrates the variability in rebound behaviour across shapes and velocities. For spheres, tested under similar conditions at the University of Newcastle,[15,16] the impact is collinear and occurs at a single point. In this case, t_I is theoretically estimated using the formulation by Deresiewicz,[69] as function of impact velocity, mass, yield stress, equivalent Young's modulus, and equivalent radius. The resulting durations (0.493, 0.480, and 0.459 ms for impact velocities of 7, 8, and 10 m/s, respectively) are significantly shorter than those observed for angular specimens. The corresponding restitution values (0.34, 0.33, and 0.31) align well with the analytical model proposed by Stronge,[70] which incorporates impact velocity, mass, yield stress, equivalent Young's modulus, and radius.

In contrast, angular specimens, particularly prisms and slabs, exhibit markedly lower restitution values and longer impact durations. This is attributed to the non-collinear nature of the impact and the presence of multiple contact points during the impact phase. Unlike spheres, which engage in a single, brief contact, angular shapes often undergo complex multi-contact interactions involving edges, vertices, and faces. This discrepancy is most pronounced for slabs and prisms, where t_I can exceed 300 ms and involve up to 8 distinct contact events, as previously discussed. These extended durations and complex contact sequences are primarily due to the geometric asymmetry of the specimens, which amplifies the effects of orientation and impact location. These interactions extend the duration of energy exchange and increase dissipation. For instance, at $v_i = 7$ m/s, median restitution values for prisms and slabs are 0.13 and 0.16, respectively, compared to 0.24 for cubes and over 0.30 for spheres.

Considering the evidence from Guccione et al.,[16] where fragmentation behaviour remained consistent across different sphere sizes when impact velocity is normalised by the critical velocity corresponding to 37% survival probability, and the similarity between our results for cubes and those reported by Das,[30] it is reasonable to expect that the general trends observed for angular blocks are likely scalable.

5. Conclusions

This study presents a comprehensive experimental investigation into the fragmentation and rebound dynamics of brittle mortar specimens resembling realistic geometries, i.e., cubes, prisms, and slabs, under free-fall impact conditions. The findings offer practical implications for rockfall propagation analysis, particularly in modelling post-impact behaviour and energy dissipation of angular blocks.

From a propagation modelling perspective, two key aspects were addressed: the occurrence of fragmentation and the rebound mechanics of intact specimens. The main conclusions to be drawn are as follows.

- Fragmentation occurrence is shape- and orientation-dependent: fragmentation has been observed to be highly sensitive to block geometry, impact location, and orientation. Cubes have exhibited the highest fragmentation threshold, fragmenting only at higher velocities and under edge impacts. Slabs and prisms have shown more frequent fragmentation, especially under eccentric

Table 10
Minimum, maximum, median (50th-percentile) values of the apparent coefficient of restitution $|v_e/v_i|$ observed in each shape for each impact velocity v_i. These values provide a quantitative basis for interpreting the trends shown in Fig. 22.

	Prism			Slab		
v_i	7 m/s			7 m/s		
	min	max	50th	min	max	50th
$\lvert v_e/v_i\rvert$	0.02	0.23	0.13	0.09	0.32	0.16
t_i (s)	0.008	0.316	0.162	0.008	0.344	0.039

Cube									
v_i	7 m/s			8 m/s			10 m/s		
	min	max	50th	min	max	50th	min	max	50th
$\lvert v_e/v_i\rvert$	0.12	0.37	0.24	0.15	0.35	0.24	0.15	0.39	0.27
t_i (s)	0.008	0.290	0.024	0.008	0.042	0.024	0.004	0.292	0.026

Sphere			
v_i	7 m/s	8 m/s	10 m/s
$\lvert v_e/v_i\rvert$	0.34	0.33	0.31
t_i (s)	$0.493 \cdot 10^{-3}$	$0.480 \cdot 10^{-3}$	$0.459 \cdot 10^{-3}$

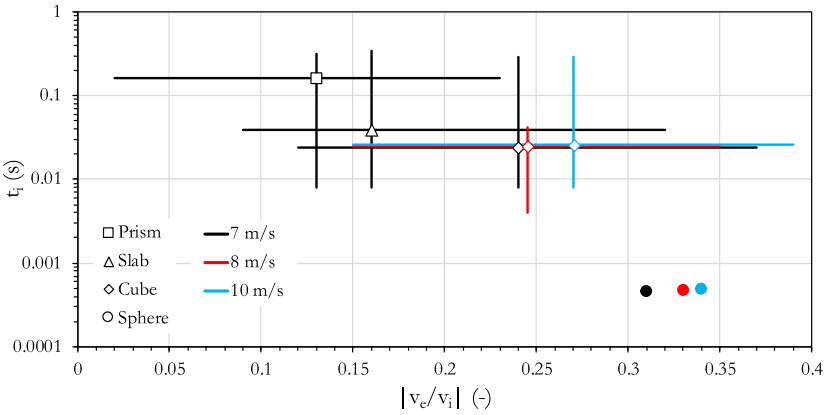

Fig. 22. Comparison of apparent coefficient of restitution ($|v_e/v_i|$) and impact duration (t_I) for prism, slab, and cube specimens at different impact velocities. Symbols represent median values, while error bars indicate minimum and maximum ranges. This visual representation complements Table 10.

impacts and when large faces are oriented parallel to the impacted surface. These findings suggest that fragmentation probability should be explicitly incorporated into trajectory models through shape-specific probabilities and orientation criteria.

- Static tests provide predictive insight into dynamic fragmentation: the fracture modes observed in static splitting tests, particularly tensile splitting and delamination, can be correlated with dynamic fragmentation behaviour. Specimens exhibiting vertex fragility or asymmetric fracture patterns under static loading are more prone to fragmentation during impact. This suggests that static mechanical characterisation can serve as a valuable tool for assessing dynamic fragility and pre-damage effects in rockfall scenarios.
- Energy dissipation and rebound mechanics are governed by contact complexity: for intact specimens, rebound behaviour has been analysed in terms of impact duration, number of contact events, and post-impact velocity components. Prisms and slabs have exhibited longer contact durations and more complex multi-contact sequences, resulting in greater energy dissipation and lower apparent restitution coefficients compared to cubes. These differences are primarily attributed to the geometric asymmetry of the specimens, which promotes uneven stress distribution and irregular contact configurations during impact. Defining an apparent coefficient of restitution has proved to be effective for non-collinear impacts, where multiple contact points and complex motion patterns challenge traditional restitution definitions. Although not a predictive model, the consistent trends observed across shapes and orientations provide a basis for anticipating impact outcomes and energy dissipation behaviour. This supports the integration of shape-dependent restitution parameters into trajectory models, enhancing their predictive capability.
- Orientation influences rebound metrics and energy partitioning: the apparent and normal restitution coefficients, as well as the vertical projection angle α, vary systematically with impact orientation and are affected by the shape.
- Rebound directionality is consistently biased yet probabilistic: across all shapes, rebound motion is predominantly aligned with the positive ξ axis, i.e., from the impact point towards the centre of gravity. However, due to the inherent unpredictability of impact orientation and contact location in real rockfall scenarios, this directionality must be treated probabilistically. The observed bias supports the use of shape-aligned local reference systems, but trajectory models should incorporate stochastic elements to account for variability in initial conditions.

Overall, the results underscore the limitations of spherical simplifications in rockfall models. The dataset provided by this study offers quantitative metrics, such as shape-dependent fragmentation probabilities and apparent restitution coefficients, that can be directly integrated into numerical rockfall models. These parameters can enable calibration of DEM and rigid-body trajectory models, replacing generic spherical assumptions and improving predictions of rebound behaviour and energy dissipation. For lumped-mass approaches, apparent restitution coefficients can be adopted to better capture non-collinear impacts. Furthermore, incorporating geometry-dependent fragmentation probabilities into stochastic fragmentation models enhances the realism of

trajectory simulations, allowing for more accurate estimation of runout distances, potential impact energies, and impact heights, and ultimately supports more reliable hazard and risk assessments[71].

Building on these results, future research will focus on deriving predictive equations that link impact conditions, block geometry, and fragmentation probability to enable direct integration into propagation models. Future studies will explicitly address size effects by testing different specimen scales and investigating whether scale-independent fragmentation patterns can be applied to angular blocks. Additional work will include testing natural rock specimens and alternative materials, as well as validating these results within numerical models to enhance predictive accuracy and strengthen hazard assessment frameworks.

CRediT authorship contribution statement

Maddalena Marchelli: Writing – review & editing, Writing – original draft, Validation, Project administration, Methodology, Investigation, Funding acquisition, Formal analysis, Data curation, Conceptualization. **Davide Ettore Guccione:** Writing – review & editing, Validation, Project administration, Methodology, Funding acquisition, Conceptualization. **Anna Giacomini:** Writing – review & editing, Project administration, Funding acquisition, Conceptualization. **Olivier Buzzi:** Writing – review & editing, Project administration, Funding acquisition, Conceptualization.

Open access

Funding

This work was supported by Marie Curie Postdoctoral Fellowship 2022 (Call Horizon-MSCA-2022-PF-01, grant GA101103401 - RIDETHERISK project), by Australian Research Council (IE230100410 and DP160103140) and Rocscience Inc.

Acknowledgements

The help received from Dr. Michele Spadari in preparing the samples and conducting the experiments is also gratefully acknowledged.

Declaration of competing interest

The authors declare that there are no conflicts of interests.

Data availability

Data supporting the findings of this study are available from the authors on request.

References

1. Hantz Didier, Corominas Jordi, Crosta Giovanni B, Jaboyedoff Michel. Definitions and concepts for quantitative rockfall hazard and risk analysis. *Geosciences*. 2021;11(4):158.
2. Rosser Nick, Massey Chris. Rockfall hazard and risk. In: *Landslide Hazards, Risks, and Disasters*. Elsevier; 2022:581–622.
3. Dorren Luuk KA. A review of rockfall mechanics and modelling approaches. *Prog Phys Geogr*. 2003;27(1):69–87.
4. Crosta GB, Agliardi F. Parametric evaluation of 3D dispersion of rockfall trajectories. *Nat Hazards Earth Syst Sci*. 2004;4(4):583–598.
5. Ma Ke, Liu Guoyang. Three-dimensional discontinuous deformation analysis of failure mechanisms and movement characteristics of slope rockfalls. *Rock Mech Rock Eng*. 2022;55(1):275–296.
6. Wyllie Duncan C. Calibration of rock fall modeling parameters. *Int J Rock Mech Min Sci*. 2014;67:170–180.
7. Caviezel Andrin, Ringenbach Adrian, Demmel Sophia E, Dinneen Claire E, Krebs Nora, Bühler Yves, Christen Marc, Meyrat Guillaume, Stoffel Andreas, Hafner Elisabeth, et al. The relevance of rock shape over mass—implications for rockfall hazard assessments. *Nat Commun*. 2021;12(1):5546.
8. Ge Yunfeng, Chen Weixiang, Ye Yang, Tang Huiming. Experimental study on the influence of morphological parameters on kinematics of rockfall trajectory. *Bull Eng Geol Environ*. 2024;83(8):324.
9. Imre B, Räbsamen S, Springman Sarah M. A coefficient of restitution of rock materials. *Comput Geosci*. 2008;34(4):339–350.
10. Asteriou P, Saroglou H, Tsiambaos G. Geotechnical and kinematic parameters affecting the coefficients of restitution for rock fall analysis. *Int J Rock Mech Min Sci*. 2012;54:103–113.
11. Asteriou Pavlos, Tsiambaos George. Empirical model for predicting rockfall trajectory direction. *Rock Mech Rock Eng*. 2016;49(3):927–941.
12. Li Li-ping, Sun Shang-qu, Li Shu-cai, Zhang Qian-qing, Hu Cong, Shi Shao-shuai. Coefficient of restitution and kinetic energy loss of rockfall impacts. *KSCE J Civ Eng*. 2016;20(6):2297–2307.
13. Wang Yanhai, Jiang Wei, Cheng Shengguo, Song Pengcheng, Mao Cong. Effects of the impact angle on the coefficient of restitution in rockfall analysis based on a medium-scale laboratory test. *Nat Hazards Earth Syst Sci*. 2018;18(11):3045–3061.
14. Sun Hanqing, Zeng Yawu, Ren Shulin, Ye Yang, Chen Xi. Breakage probability of marble spheres under normal, repeated impacts. *Int J Impact Eng*. 2019;130:68–78.
15. Guccione Davide Ettore, Buzzi Olivier, Thoeni Klaus, Fityus Stephen, Giacomini Anna. Predicting the fragmentation survival probability of brittle spheres upon impact from statistical distribution of material properties. *Int J Rock Mech Min Sci*. 2021;142:104768.
16. Guccione Davide Ettore, Giacomini Anna, Thoeni Klaus, Fityus Stephen, Buzzi Olivier. On the dynamic fragmentation of rock-like spheres: insights into fragment distribution and energy partition. *Rock Mech Rock Eng*. 2023;56(2):847–873.
17. Ji Zhong-Min, Zhang Huan-Huan, Saroglou Haris, Asteriou Pavlos, Wang Ting-Hui, Wang Dong-Po, Wu Fa-Quan, Li Zhen-Hua. Three decades in review: The evolution of rockfall impact testing apparatuses. *Rock Mech Rock Eng*. 2025:1–26.
18. Marchelli Maddalena, Guccione Davide Ettore, Giacomini Anna, Buzzi Olivier. Fragmentation patterns and trajectories during rockfall: Analysis of the influence of discontinuities and impact conditions through drop tests: M. Marchelli et al.. *Rock Mech Rock Eng*. 2025:1–33.
19. Chau Kam Tim, Wong RHC, Wu JJ. Coefficient of restitution and rotational motions of rockfall impacts. *Int J Rock Mech Min Sci*. 2002;39(1):69–77.
20. Li Li-ping, Sun Shang-qu, Li Shu-cai, Zhang Qian-qing, Hu Cong, Shi Shao-shuai. Coefficient of restitution and kinetic energy loss of rockfall impacts. *KSCE J Civ Eng*. 2016;20:2297–2307.
21. Asteriou Pavlos, Tsiambaos George. Effect of impact velocity, block mass and hardness on the coefficients of restitution for rockfall analysis. *Int J Rock Mech Min Sci*. 2018;106:41–50.
22. Wittel Falk K, Carmona Humberto A, Kun Ferenc, Herrmann Hans J. Mechanisms in impact fragmentation. *Int J Fract*. 2008;154:105–117.
23. Carmona Humberto A, Wittel Falk K, Kun Ferenc, Herrmann Hans Jürgen. Fragmentation processes in impact of spheres. *Phys Rev E*. 2008;77(5):051302.
24. Buzzi Olivier, Guccione Davide Ettore. An analytical model to predict the survival probability of irregular brittle rocks in rockfall under collinear impact. *Rock Mech Rock Eng*. 2023;56(6):4659–4665.
25. Buzzi Olivier, Giacomini Anna, Spadari Michele. Laboratory investigation on high values of restitution coefficients. *Rock Mech Rock Eng*. 2012;45(1):35–43.
26. Krengel Dominik, Shiyake Ryota, Kikumoto Mamoru. Effect of particle shape and initial orientation on the kinematics and runout behavior of rockfalls. *Landslides*. 2024;21(8):1797–1809.
27. Dattola G, di Prisco C, Crosta GB. Modeling ellipsoidal block impacts by an advanced rheological model. *Rock Mech Rock Eng*. 2023;56(11):7997–8018.
28. Scaravaglione Giulio, Latham John-Paul, Xiang Jiansheng. Numerical model study of prototype drop tests on cube and cubipod® concrete armor units using the combined finite–discrete element method. *J Mar Sci Eng*. 2021;9(5):460.

29. Yu Wenxuan, Jin Liu, Du Xiuli, Deng Xiaofang. Effect of initial damage state on static and dynamic fracture of concrete with different sizes: an experimental study. *Eng Fract Mech*. 2022;274:108797.
30. Das Rajarshi, Cleary PW. Effect of rock shapes on brittle fracture using smoothed particle hydrodynamics. *Theor Appl Fract Mech*. 2010;53(1):47–60.
31. Ye Yang, Li Changdong, Zeng Yawu, Tang Huiming. Modelling dynamic breakage in rock blocks with different elongation and flatness ratios upon impact. *Int J Numer Anal Methods Geomech*. 2024;48(3):771–792.
32. Giacomini A, Buzzi O, Renard B, Giani GP. Experimental studies on fragmentation of rock falls on impact with rock surfaces. *Int J Rock Mech Min Sci*. 2009;46(4):708–715.
33. Spadari M, Giacomini A, Buzzi O, Fityus S, Giani GP. In situ rockfall testing in new south wales, Australia. *Int J Rock Mech Min Sci*. 2012;49:84–93.
34. Gili JA, Ruiz-Carulla Roger, Matas G, Moya J, Prades A, Corominas J, Lantada Nieves, Núñez Andrés María Amparo, Buill F, Puig C, et al. Rockfalls: Analysis of the block fragmentation through field experiments. *Landslides*. 2022;19(5):1009–1029.
35. Volkwein Axel, Brügger Lucas, Gees Fabio, Gerber Werner, Krummenacher Barbara, Kummer Peter, Lardon Jessica, Sutter Tobias. Repetitive rockfall trajectory testing. *Geosciences*. 2018;8(3):88.
36. Caviezel Andrin, Demmel Sophia E, Ringenbach Adrian, Bühler Yves, Lu Guang, Christen Marc, Dinneen Claire E, Eberhard Lucie A, von Rickenbach Daniel, Bartelt Perry. Reconstruction of four-dimensional rockfall trajectories using remote sensing and rock-based accelerometers and gyroscopes. *Earth Surf Dyn*. 2019;7(1):199–210.
37. Guccione DE, Thoeni K, Giacomini A, Buzzi O, Fityus S. Efficient multi-view 3D tracking of arbitrary rock fragments upon impact. *Int Arch Photogramm Remote Sens Spat Inf Sci*. 2020;43:589–596.
38. Leine Remco I, Schweizer Andreas, Christen Marc, Glover James, Bartelt P, Gerber Werner. Simulation of rockfall trajectories with consideration of rock shape. *Multibody Syst Dyn*. 2014;32:241–271.
39. Glover James, Bartelt Perry, Christen Marc, Gerber Werner. Rockfall-simulation with irregular rock blocks. In: *Engineering Geology for Society and Territory-Volume 2: Landslide Processes*. Springer; 2015:1729–1733.
40. Li Langping, Lan Hengxing. Probabilistic modeling of rockfall trajectories: a review. *Bull Eng Geol Environ*. 2015;74:1163–1176.
41. Ruiz-Carulla Roger, Corominas Jordi, Mavrouli Olga. A fractal fragmentation model for rockfalls. *Landslides*. 2017;14(3):875–889.
42. Matas Gerard, Lantada Nieves, Corominas Jordi, Gili Josep, Ruiz-Carulla Roger, Prades Albert. Simulation of full-scale rockfall tests with a fragmentation model. *Geosciences*. 2020;10(5):168.
43. Matas Gerard, Lantada Nieves, Corominas Jordi, Gili Josep A, Ruiz-Carulla Roger, Prades Albert. RockGIS: a GIS-based model for the analysis of fragmentation in rockfalls. *Landslides*. 2017;14(5):1565–1578.
44. Wang Yuannian, Tonon Fulvio. Discrete element modeling of rock fragmentation upon impact in rock fall analysis. *Rock Mech Rock Eng*. 2011;44:23–35.
45. Lanfranconi Camilla, Frattini Paolo, Sala Gianluca, Dattola Giuseppe, Bertolo Davide, Sun Juanjuan, Crosta Giovanni Battista. Accounting for the effect of forest and fragmentation in probabilistic rockfall hazard. *Nat Hazards Earth Syst Sci*. 2023;23(6):2349–2363.
46. Guccione Davide Ettore, Barros Guilherme, Thoeni Klaus, Huang Zhanyu, Giacomini Anna, Buzzi Olivier. A new stochastic rockfall fragmentation approach for lumped mass simulations. *Rock Mech Rock Eng*. 2025:1–34.
47. Guccione Davide Ettore, Thoeni Klaus, Fityus Stephen, Nader François, Giacomini Anna, Buzzi Olivier. An experimental setup to study the fragmentation of rocks upon impact. *Rock Mech Rock Eng*. 2021;54(8):4201–4223.
48. Bieniawski ZT, Hawkes I. Suggested methods for determining tensile strength of rock materials. *Int J Rock Mech Min Sci*. 1978;15(3):99–103.
49. British Standards Institution. BS 1881-117:1983 testing concrete – method for determination of tensile splitting strength. 1983 Superseded by BS EN 12390-6:2000.
50. European Committee for Standardization. EN 12390-6:2023 testing hardened concrete – part 6: Tensile splitting strength of test specimens. 2023.
51. ASTM International. ASTM C496/C496M-17 standard test method for splitting tensile strength of cylindrical concrete specimens. 2017.
52. ASTM International. ASTM D3967-16 standard test method for splitting tensile strength of intact rock core specimens. 2022.
53. Chitharanjan N, Sundararajan R, Manoharan P Devadas. Development of aerocrete: a new lightweight high strength material. *Int J Cem Compos Light Concr*. 1988;10(1):27–38.
54. Ince Ragip. Determination of concrete fracture parameters based on peak-load method with diagonal split-tension cubes. *Eng Fract Mech*. 2012;82:100–114.
55. Ince Ragip, Gör Mesut, Alyamaç Kürşat Esat, Eren Mehmet Esen. Multifractal scaling law for split strength of concrete cubes. *Mag Concr Res*. 2016;68(3):141–150.
56. Nguyen Thi-Thuy-Hang, Mai Hong-Ha, Phan Duc-Hung, Nguyen Duy-Liem. Responses of concrete using steel slag as coarse aggregate replacement under splitting and flexure. *Sustainability*. 2020;12(12):4913.
57. Sharaky Ibrahim A, Elamary Ahmed S, Alharthi Yasir M. Effect of waste basalt fines and recycled concrete components on mechanical, water absorption, and microstructure characteristics of concrete. *Materials*. 2022;15(13):4385.
58. Wijk Gunnar. The point load test for the tensile strength of rock. *Geotech Test J*. 1980;3(2):49–54.
59. Alshkane Younis M, Hama Saeed Safin Bahadin. Effect of freezing and thawing on physical and mechanical properties of sedimentary rock. *J Garmian Univ*. 2018;5(2):126–140.
60. TEMA. Image systems motion analysis, TEMA 3D. 2019 http://www.imagesystems.se/tema/.
61. The MathWorks Inc. MATLAB version: 9.13.0 (R2023b). 2023 URL https://www.mathworks.com.
62. Vijayakumar S, Yacoub Thamer, Ranjram M, Curran JH. Effect of rockfall shape on normal coefficient of restitution. In: *ARMA US Rock Mechanics/Geomechanics Symposium*. ARMA; 2012 ARMA–2012.
63. Hiramatsu Yoshio, Oka Yukitoshi. Determination of the tensile strength of rock by a compression test of an irregular test piece. In: *International Journal of Rock Mechanics and Mining Sciences & Geomechanics Abstracts*. Elsevier; 1966:89–90. vol. 3, 2.
64. Broch E, Franklin JA. The point-load strength test. In: *International Journal of Rock Mechanics and Mining Sciences & Geomechanics Abstracts*. Elsevier; 1972:669–676. vol. 9, 6.
65. Bieniawski ZT, Bernede MJ. Suggested methods for determining the uniaxial compressive strength and deformability of rock materials: Part 1. Suggested method for determining deformability of rock materials in uniaxial compression. In: *International Journal of Rock Mechanics and Mining Sciences & Geomechanics Abstracts*. Elsevier; 1979:138–140. vol. 16, 2.
66. Kuruppu Mahinda D, Obara Yuzo, Ayatollahi Majid R, Chong KP, Funatsu Takahiro. ISRM-suggested method for determining the mode I static fracture toughness using semi-circular bend specimen. *Rock Mech Rock Eng*. 2014;47:267–274.
67. Angelidakis Vasileios, Nadimi Sadegh, Utili Stefano. Elongation, flatness and compactness indices to characterise particle form. *Powder Technol*. 2022;396:689–695.
68. Zingg Theodor. *Beitrag zur Schotteranalyse* [Ph.D. thesis]. ETH Zurich; 1935.
69. Deresiewicz Herbert. Stresses in beams having holes of arbitrary shape. *J Eng Mech Div*. 1968;94(5):1183–1214.
70. Stronge William James. *Impact Mechanics*. Cambridge University Press; 2018.
71. Marchelli Maddalena, De Biagi Valerio, Chiaia Bernardino. A fully probabilistic framework to compute the residual rockfall risk in presence of mitigation measures. *Landslides*. 2024:1–8.